Paper Physics

John Considine*, D. Steven Keller, Matthew A. Arvanitis and Xiaoyan Tang

Heterogeneity characterization of commercial structural papers

https://doi.org/10.1515/npprj-2023-0080
Received November 22, 2023; accepted March 18, 2024;
published online April 9, 2024

Abstract: Evaluation of physical and mechanical heterogeneity in commercial paperboards is needed to promote their use in structural applications, especially within the field of packaging. Understanding the range of their behaviors is needed to compete with other materials in the current marketplace and expand in others. This work describes the physical and stiffness heterogeneities of twelve commercial materials using tensile tests in the cross-machine direction and several inverse analyses. The effects of grammage, thickness, and apparent density on tensile stiffness were evaluated in both the linear elastic and nonlinear regimes. Thickness and density provided the best explanation for elastic heterogeneous behavior in most of the materials; local grammage was not the best descriptor for any material. The analyses used here were not able to provide a good explanation of the nonlinear behavior, which was attributed to the development of large shear strains within the materials as they neared failure. This work provides a methodology for additional heterogeneous behavior examinations.

Keywords: grammage; heterogeneity; paperboard; profilometry; VFM

1 Introduction

Packaging-grade papers, such as linerboards, medium, and sack papers, are green materials that are used to transport and protect products when moving from manufacturers to assemblers and consumers. Especially in the case of corrugated board, the manufacturing plant needs to be near the facilities that create the product due to the expense of transporting the light but bulky board. Therefore, these plants are spread throughout industrial regions, thereby providing employment and strengthening local economies. To maintain market share in this segment and compete in other material markets, continual improvements in these materials are an ongoing area of research. One such improvement is reduction of weight while maintaining strength.

One significant challenge unique to cellulose products is their heterogeneity at multiple length scales. This heterogeneity can make competing in specialty markets, e.g., medical component packaging, particularly demanding. In these types of applications, the packaging must work 100 % of the time. Overdesign generally involves additional fiber, the most expensive component in the papermaking process.

For these materials, the effect of different types of heterogeneity is not well understood. At the macroscopic length scale (>cm), the material will have some combination of grammage (weight/area), thickness, residual stress, and fiber orientation differences. As we will directly present, researchers have developed techniques to examine these properties and characterize various types of heterogeneities. The spatial variation of grammage is called formation; a region with an aggregation of fibers is called a floc, and a region of low grammage is called a light-weight zone.

Differences in local fiber orientation contribute to anisotropy. Dias et al. (2023) developed a method to measure surface fiber orientation on a 4 cm^2 region. Enomae et al. (2008) used confocal laser scanning microscopy to examine the z-direction distribution of in-plane ($x - y$) fiber orientation. These orientation changes are attributed to shearing and turbulence in the headbox and differential speed of wire and pulp jet (Schaffnit et al. 1992). The fibrous structure contributes to mass and thickness variations, but because it is compressible, measurement of thickness variation is challenging (Sampson 2009).

The in-plane distribution of mass, or formation, in papers and paperboards is the result of the fiber furnish, especially fiber length (Kerekes and Schell 1992, 1995), and the turbulent energy introduced by the headbox and elements in the forming section before the wet web is

***Corresponding author: John Considine**, USDA, Forest Service, Forest Products Laboratory, Madison, WI, USA, E-mail: john.considine@wisc.edu. https://orcid.org/0000-0001-6123-399X
D. Steven Keller, Miami University, Oxford, OH, USA, E-mail: kellerds@miamioh.edu
Matthew A. Arvanitis and Xiaoyan Tang, USDA, Forest Service, Forest Products Laboratory, Madison, WI, USA, E-mail: matthew.arvanitis@usda.gov (M.A. Arvanitis), xiaoyan.tang@usda.gov (X. Tang)

immobilized (Norman and Söderberg 2001; Sampson 2001). For paperboards made using multiple forming sections, the in-plane distribution of mass becomes even more complex. As such, paperboard products may exhibit a wide spectrum of floc size and intensity in the observed formation (Abedsoltan et al. 2016). The in-plane distribution of mass is typically mapped using transmission of light or higher energy radiography. In the case of unfilled paperboards with mean grammage greater than 120 g m^{-2}, precise measurement of grammage to in-plane dimensions of 100 μm or less is possible using transmission radiographic imaging using soft X-rays as the source (Abedsoltan et al. 2016). Pointwise mapping of higher grammage paperboard has been performed using ^{147}Pm β-ray as a source. A more recent method of mapping using tera-hertz time-domain spectroscopy, providing a resolution of ~600 μm, was introduced by Missori et al. (2015) with an instrument developed at Papiertechnische Stiftung (Krok et al. 2023).

Tensile strength is one of the most common specifications for paper and paperboards, therefore many researchers have tried to relate heterogeneity to strength, with mixed results. Examining laboratory-made, low grammage materials (60 g m^{-2}) under tension, Villette et al. (2022) observed smaller strains in flocs than in light-weight zones and attributed their strain differences to thickness differences because they had similar bulk porosities. Examining grammage maps of copy paper, Na and Muhlstein (2019) recorded changes in floc geometry due to loading direction. High-strain regions were not the same shape as the flocs, and anisotropic behavior was caused by fiber orientation relative to loading direction. Imaging coated papers using 4D synchrotron X-ray tomography during tensile tests showed that cross-machine direction (CD) failure is ductile, due to breaking of fiber-fiber bonds, and fibers tended to align in the direction of applied load (Johansson et al. 2022). For materials made in a laboratory sheetformer, global in-plane elastic properties were insensitive to grammage variation. However, they found tensile strength decreased with increased grammage variation (Waterhouse et al. 1991). Considering machine-made papers, Moffatt et al. (1973) found that failure occurred in regions of low grammage. However, Mohlin (2001) found no relationship between grammage variation and specific tensile strength. Nordström (2003) found that a relationship between strength and grammage variation was dependent on mean grammage and bonding. Wathén and Niskanen (2006) found a weak correlation between tensile strength and grammage variation. Lahti et al. (2020) found that grammage variation was a good failure predictor for their 73 g m^{-2} kraft paper.

The continuous improvement of full-field displacement measurements have encouraged their use on cellulose materials for the examination of local behavior. Holography (Lyne and Hazell 1973), digital image correlation (DIC) (Chao and Sutton 1988; Sutton and Chao 1988; Wong et al. 1996), and confocal microscopy (Ting et al. 1998) have been used to examine tensile behavior of cellulose materials. For handsheets, works have reported an inverse relationship between strain and grammage and failure at low grammage regions (Wong et al. 1996), and large strains as failure precursors at the millimeter scale (Borodulina et al. 2012).

This work is part of Material Testing 2.0 (MT2.0) (Pierron and Grédiac 2021) research that involves the design and optimization of mechanical tests for identification of mechanical constitutive parameters. The goal of that effort is to collect more data from a single test, thereby reducing test effort and improving the quality of material models. To that end, the work described herein is an extension of earlier work (Considine et al. 2017), that employed a tensile test configuration with a special specimen geometry and loading schedule. This extension involves the investigation of several commercial materials, incorporation of local physical properties, and a comparison of different inverse methods. Whereas previous efforts (Johansson et al. 2022; Lahti et al. 2020; Moffat et al. 1973; Nordström 2003; Waterhouse et al. 1991; Wathén and Niskanen 2006) focused on local strain and strength, this work incorporated identification of local stiffness as an additional measurement to characterize material heterogeneity.

Although that earlier work (Considine et al. 2017) used different virtual fields method (VFM) techniques, some of which were used here, we also incorporated finite element model updating (FEMU) that has widespread utilization. Alzweighi et al. (2021) used FEMU to examine machine direction (MD) tensile response of sack papers. In that work, heterogeneity of the strain field was caused by local density variations. However, mechanical response was dominated by fiber orientation. Also using FEMU for a biaxially tensile loaded specimen, but on sketch paper and paperboard, Ostoja-Starzewski and Castro (2003) found interaction between grammage variation and strain and estimated a representative volume element on the order of 10× larger than the floc size.

The objective of this work was to characterize the heterogeneity of commercial paperboards to determine the source of non-uniform mechanical response and whether the observed heterogeneity is physical or mechanical. The materials examined here have higher grammages than much of the previous work that focused on laboratory paper and/or material less than 75 g m^{-2} (Enomae et al. 2008; Krasnoshlyk et al. 2018; Lyne and Hazell 1973; Moffat et al. 1973; Na and Muhlstein 2019; Ting et al. 1998; Villette et al. 2022; Waterhouse et al. 1991). Moreover, rather than relying

on tensile strength as the only mechanical metric, we have incorporated local stiffness. Tensile failure occurs less than buckling failure for these materials in their end use, usually corrugated board, and buckling is primarily controlled by stiffness. It is anticipated that this information will help papermakers determine if changes to their process are cost effective. Additionally, this work provides information that can help improve production processes that affect mechanical performance of green materials to better compete in the global materials product space.

After a description of materials, we explain our measurements of local grammage and thickness. Tensile tests were used to provide mechanical behavior data. A significant portion of this paper describes the methods applied to identify local stiffness with respect to physical properties and how to rank the effectiveness of those methods.

2 Materials

Orthotropy ratio (OR), grammage, thickness, apparent density, and ash content for the commercial materials examined in this work are listed in Table 1. The samples presented here are a subset of a larger study that examined 26 different papers and paperboards and characterized the heterogeneity of three specimens for each material. This subset was selected based on two criteria: they had good stiffness identification, using a metric defined in Section 4.5, and failure occurred away from the edge of the specimen. Orthotropy ratio is included to provide some additional information on mechanical behavior, since this work includes CD mechanical behavior only.

Material W was a filter paper and the only non-structural material. It was manufactured by Whatman® International (Maidstone, Kent, UI) and identified as Chromotography Paper, Model 3MM CHR. It was included as a reference material for researchers because the other materials in this work came from industrial cooperators and could not be duplicated for future work. This material was assumed to be generally homogeneous, with low density and only trace (<0.01 %) inorganic content.

The commercial samples were expected to contain low amounts of mineral matter measured as ash that may have entered the stock stream through the recovered fiber content. Since minerals will have a different absorption coefficient than cellulose for the X-radiation, it was important to establish the extent to which radiographic results would be influenced. To this end, ash content, fired at 900 °C, was determined for each sample, as shown in Table 1. All materials, with exception of Materials L and P had ash samples less than 2 %. In all cases, mineral matter was detected in radiographs as high-density spots with diameters generally <50 µm. Since mineral matter has much higher density than the fibers, the spots occupied only a small fraction of the grammage map. Therefore, the ash content was deemed insignificant to the statistical and the cross-correlation analyses.

3 Methods

Both physical and mechanical heterogeneity were examined. Physical heterogeneity examination included local thickness, grammage, and apparent density. Mechanical heterogeneity involved tensile testing of CD specimens.

3.1 Thickness & grammage

Grammage was mapped in two dimensions using soft X-radiographic imaging described by Abedsoltan et al. (2016). The traditional β-radiographic methods for mapping paper formation by contacting with ^{14}C doped PMMA plates (Cresson et al. 1990; Keller and Pawlak 2001) was considered unsuitable for use in this study because the samples exceeded the maximum penetration grammage of about 120 g m^{-2}. Also, the

Table 1: Mean physical properties of materials examined in this work. COV is coefficient of variation; *K* and *S* are kurtosis and skewness, respectively, of the particular distribution. Column 'OR' refers to orthotropy ratio, Q_{11}/Q_{22}. OR values with (*) were taken from Considine et al. (2011); those unmarked were taken from unpublished ultrasonic data.

Material	Type	OR	g g m^{-2}	COV(g) %	$K(g)$	$S(g)$	t µm	COV(t) %	$K(t)$	$S(t)$	ρ kg m^{-3}	COV(ρ) %	$K(\rho)$	$S(\rho)$	Ash (%)
A	Linerboard	*2.10	269	11	0.42	0.38	314	8	0.27	0.25	855	6	0.30	0.14	1.12
E	Linerboard	*2.08	209	10	−0.03	0.33	256	4	−0.27	−0.28	818	11	0.35	0.73	1.17
F	Linerboard	1.84	222	7	0.22	−0.02	278	6	0.37	−0.46	800	5	0.52	0.08	1.03
G	Medium	2.35	120	22	1.58	0.21	118	20	1.17	−0.65	1019	10	7.55	1.88	1.68
I	Medium	3.44	163	9	0.75	0.39	173	8	0.17	−0.03	943	6	0.70	0.36	1.70
J	Medium	3.66	166	9	1.84	0.65	167	9	0.21	−0.06	998	5	1.28	0.74	1.62
K	Medium	2.77	157	12	−0.13	0.12	157	13	−0.13	0.08	1003	5	0.34	0.27	0.84
L	Medium	3.89	165	9	0.05	0.13	200	8	−0.31	−0.25	825	4	1.53	0.52	2.18
P	Medium	4.56	172	14	0.41	0.36	219	7	−0.15	−0.14	783	9	0.87	0.46	2.33
S	Sack paper	1.84	69	16	0.29	0.40	59	17	0.37	0.28	1179	10	3.70	0.64	0.83
T	Sack paper	1.65	90	15	−0.17	0.26	79	15	0.00	−0.10	1160	18	2.32	1.25	0.88
W	Filter paper	*2.13	183	7	0.26	0.39	294	6	0.52	0.25	623	3	0.17	−0.02	0.00

geometry of contact radiography causes the loss of depth of field and resolution of structural features as a function of thickness (Keller and Pawlak 2001). A Minishot X-ray cabinet (Associated X-ray Corporation, East Haven, CT) was used to generate a 6 kV and 4.5 mA conical beam of low-energy (soft) X-ray. Dog bone samples were placed directly on X-ray film (Structurix D2, Agfa) to optimize imaging sharpness. Exposures of all samples included a step wedge with five thicknesses of Mylar placed adjacent to samples for use as an internal grammage reference. Grammage maps were determined based on the method developed by (Feng 2012; Keller et al. 2013). Film was developed and scanned in transmission using a desktop scanner (Perfection V800, Epson) at a resolution of 4800 dpi, producing a practical resolution ~10 µm considering all aspects of the radiographic process. Vignette correction was performed to compensate for the intensity gradient caused by the source-detector geometry. Figure 1 shows an example of the grammage data.

Thickness mapping was performed using the Twin Laser Profilometry (TLP) method introduced by Sung et al. (2005). Both sides of each sample were raster scanned using two opposing laser range sensors. The simultaneous range measurements obtained distance by triangulation to a precision of 1 µm in three dimensions. The difference between the two surface points in the *z*-direction, normal to the principal plane of the sample, was used to calculate the thickness at a given point within the *x*–*y* plane. An array of locations spaced 200 µm apart in the *x*–*y* plane was mapped. After precise alignment of the grammage and thickness maps using imaging software, the local apparent volumetric density was calculated for each thickness location by reducing the local grammage values by the corresponding local thickness. The three structural maps were also precisely aligned with the printed pattern used in strain mapping experiments.

Thickness was also measured using the TAPPI Standard Method T-411 (TAPPI 2015). For samples with considerable thickness variation, values of thickness obtained from thickness measurements are typically greater than mean thickness values calculated from mapping methods that use probes with test areas finer than the scale of the surface and thickness irregularity. This was demonstrated by Fellers et al. (1986) with opposing contacting spheres and (Sung et al. 2005) using laser spot diameter, as in the present case, providing values approaching true thickness. By contrast, caliper methods such as TAPPI T-411 are unable to contact the full surface over the 13 mm diameter platen area. By neglecting the thinnest regions, the apparent thickness measured tends to be higher than the true thickness. This also has implications for calculating density values that will be greater than those calculated using the TAPPI Standard methods.

As a result of the low values of mineral matter (ash) contained in the materials, and the insignificant influence this has on the overall areal distribution of radiographic absorption, a uniform correction of grammage was applied to each data set during conversion from pixel gray level to local grammage. The uncorrected mean radiographic grammage could differ considerably from the TAPPI Standard Grammage of Paper and Paperboard, T-410 (TAPPI 2023), by as much as 40 g m^{-2} for specimens with 2 % ash content (Abedsoltan et al. 2016). To provide a more accurate representation of local grammage based on the fiber content within each pixel region, radiographic data sets were uniformly corrected to the mean gravimetric grammage. This resulted in realistic values for local density, except for the very few pixels that contained mineral content.

3.2 Tensile testing

Tensile specimens had the same dog bone geometry as used by Considine et al. (2017); the central active area was 44 mm wide and 140 mm long. The active area of the dog bone geometry used in this study was larger than many dog bone geometries used in other studies to better capture its heterogeneous behavior. These tests were performed on an Instron® (Norwood, Massachusetts) Model 5865 test machine equipped with serrated-face pneumatic grips. The testing direction for all specimens was the 2-material direction, also called the CD, and was chosen because it is the most common load direction in structural paperboard applications. Figure 2 shows a dog bone specimen for Material P with DIC pattern. Application of the pattern is presented in Section 3.3.

Figure 3 shows the tensile test for Material A. Initiation of the test schedule began with an increase of the load from null to 0.23 kN m^{-1}

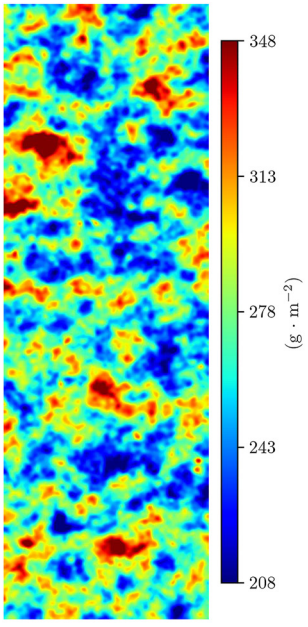

(a) Contour plot of grammage.

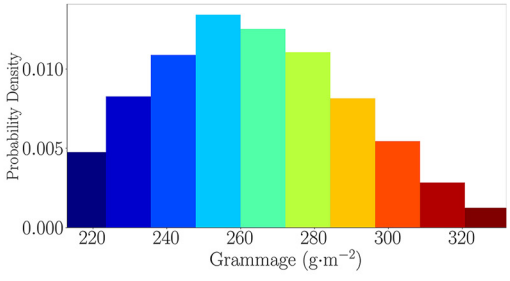

(b) Grammage histogram.

Figure 1: Example grammage data for Material A.

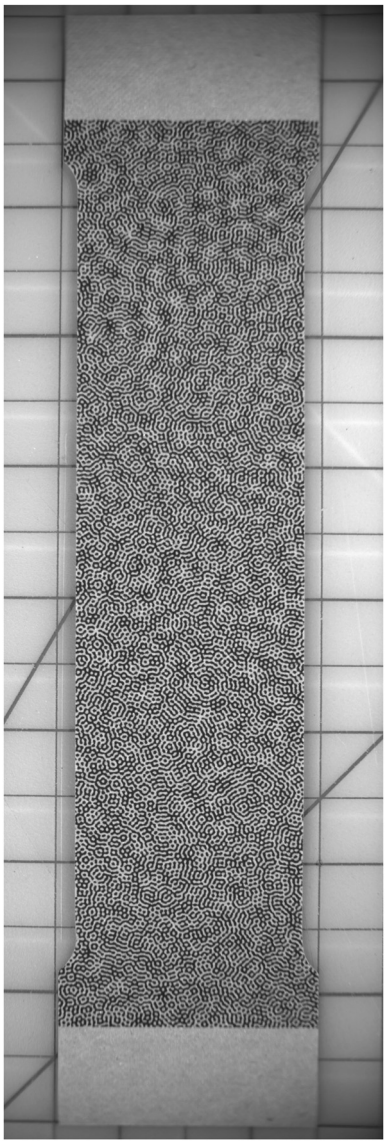

Figure 2: Image of Material P dog bone specimen with DIC pattern. Background grid are 12.5 mm squares. Angle lines are at 45° and 60°.

(10 N) and a hold for 50 s; the null load portion is not shown in the figure. After this initial hold, the load was increased to 2.73 kN m^{-1} (120 N) and held for 50 s. Subsequent hold periods alternate between 0.23 kN m^{-1} (10 N) and 2.27 kN m^{-1} (100 N). The loading and unloading rates were ± 150 N min^{-1}. After 5 cycles, the load was increased from 2.27 kN m^{-1} at 3 mm min^{-1} until tensile failure. Data capture (load and grip displacement) and image capture were synchronized and occurred at 1 Hz.

Figure 4 shows the same tensile test as in Figure 3, but with load versus mean DIC ε_y. The load cycles 2–5 did have a small amount of hysteresis, but were repeatable and had similar stiffnesses, represented by the slope of these data, to each other and to the first cycle.

For each material, the loads for each cycle were selected such that the material would remain in the elastic regime. The first load cycle was either 5 N or 10 N higher than subsequent cycles to relieve some internal residual stresses. Higher load in the initial load cycle was used to increase the repeatability of the later load cycles, i.e., we were trying to avoid the potential release of residual stresses with each cycle. Although it was not known if the materials had significant residual stresses, this pre-load conditioning provided a common load history for each specimen. Additionally, each specimen was moisture conditioned at 30 % RH, 80 °C for 24 h and re-conditioned at 50 % RH, 23 °C for 24 h before testing.

Cycles 1–5 were performed with load control. By using a higher load for cycle 1, residual stresses were released so that cycles 2–5 had very similar strain behavior. In Considine et al. (2017) the strain similarity from cycle to cycle was demonstrated by turning the specimen top-to-bottom after five cycles and performing another five cycles and comparing the strain contours for each cycle.

3.3 Digital image correlation

Table 2 lists the specifications of the stereo DIC system that was used to examine the surface of the specimens during tensile testing. An optimized random grey level pattern, as given by Bossuyt (2013), was copied onto each specimen using a Sharp® (Sharp Electronics Corp., Mahwah, NJ) MX-3100N copier. Identification of varying local stiffness requires high strain accuracy and resolution as provided by stereo digital image correlation.

At each hold period 50 images were captured and averaged to create a single image to mitigate the effect of random gray level noise. Image averaging is an accepted DIC practice. The images averaged at 10 N load were used as the reference images; each specimen had six reference images. The analyzed images for the five load cycles were the image average of those captured during the hold period at the specified higher load levels, which varied for each material. For the final portion of the test the reference image was the average of images captured at the final 10 N hold period and the analyzed image was a single image captured immediately prior to tensile failure. The variation of $\underline{\varepsilon_y}$ of the 50 images was almost entirely within the strain resolution in Table 2.

4 Inverse methodology

Inverse methodologies are a category of analysis in solid mechanics in which constitutive parameters and stresses are identified from specimen geometry, given forces at known locations over certain boundaries, full field displacements, and analytical expression of constitutive equations. The present work used three different inverse methods, a Fourier-based Virtual Field Method (FVFM), FEMU, and an equilibrium gap (EG) method. Each of these methods is a type of a Virtual Fields Method (VFM). VFM was developed from the Principle of Virtual Work (PVW) (Pierron and Grédiac 2012) and, for a plane stress problem, can be written with material coordinates as:

$$\int_S (\sigma_1\varepsilon_1^* + \sigma_2\varepsilon_2^* + \sigma_6\varepsilon_6^*)dS = \int_{\partial S} T_i u_i^* dl \qquad (1)$$

where S is the area of 2-D domain, σ_i are stresses (with Voigt notation) within S, u_i^* are continuous and piecewise

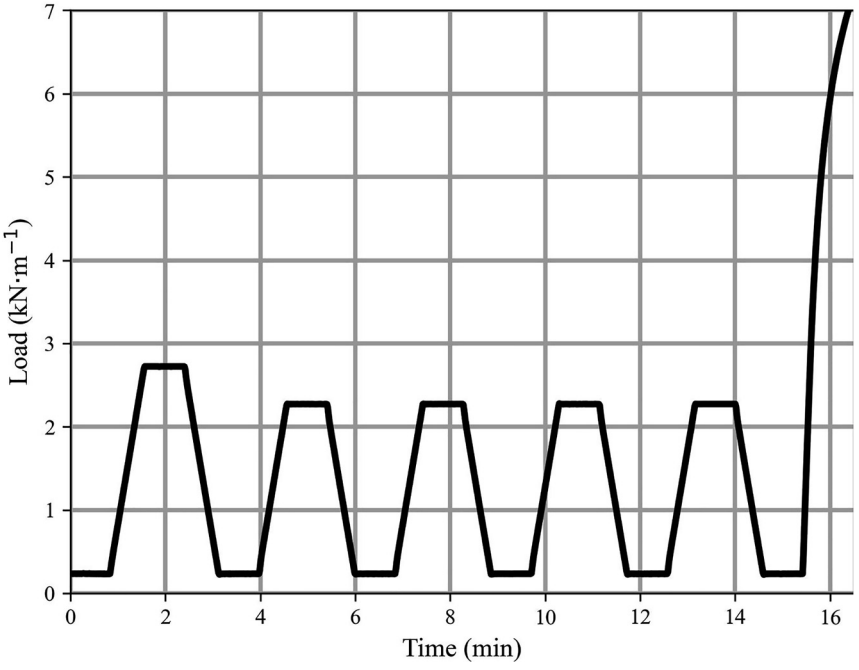

Figure 3: Example tensile test - Material A.

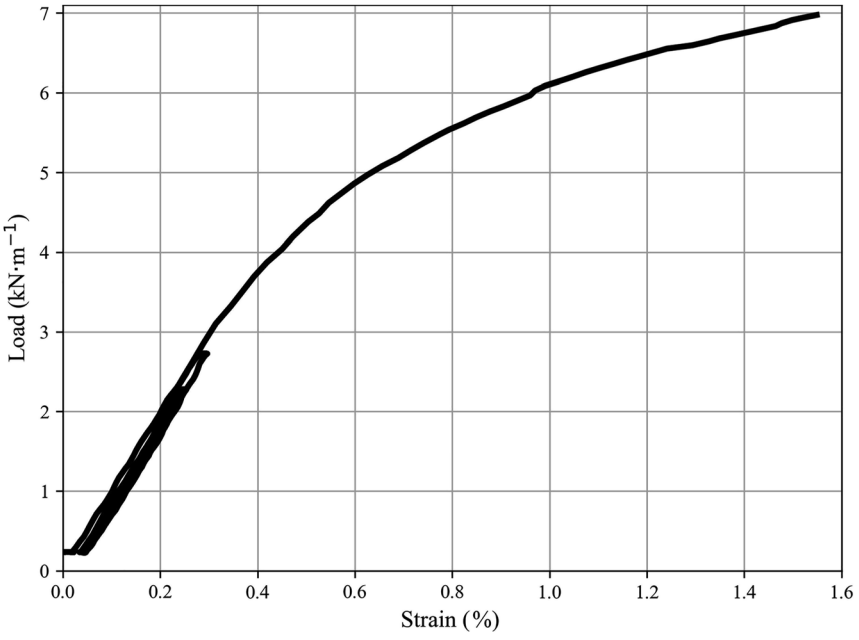

Figure 4: Example tensile test for Material A showing load versus strain, where strain is the mean ε_y as determined by DIC.

differentiable virtual displacements, ε_i^* are virtual strains associated with u_i^*, T_i are tractions on ∂S, and ∂S is the boundary of S over which non-zero tractions T_i exist.

Application of Equation (1) requires the use of a constitutive relation to write the PVW in terms of measurable quantities, ε_i in this case, and the unknowns we are trying to identify, Q_{22} and Q_{12}. A uniaxial tensile test of a homogeneous linear elastic orthotropic material performed in the y-direction (CD in this work) contains information to identify Q_{22} and Q_{12} only because $\sigma_6 = 0$. Q_{66} is an independent material property for orthotropic materials, and a uniaxial tensile test will not activate σ_6 for Q_{66} identification. Furthermore, because the material coordinates (1, 2) are aligned with the spatial coordinates (x, y) for this work, subsequent notation will use spatial coordinates. Identification was evaluated in the linear elastic regime using a linear elastic isotropic constitutive equation given by

Table 2: Technical information about the DIC equipment, set-up, and system.

Parameter	Setting
Technique	Stereo image correlation
Cameras	Stingray model F504B
Lens	Computer (Commack, NY) M1614-MP2, 16 mm, f1.4
Imaging distance	0.373 m
Lighting	White fluorescent
Resolution	2452 · 2056, 12-bit
Noise	0.4 % of dynamic range
Software	MatchID v2022.2.1
Capture rate	1.0 Hz
Pixel to mm conversion	1 pixel = 0.036 mm
ROI	140 mm · 44 mm
Subset, step	21, 10 (pixels)
Displacement, in-plane resolution	0.021 pixels, 0.39 µm
Strain	
Calculation	Improved quadratic quadrilateral
Strain window	9 data points
VSG, virtual strain gage	101 pixels, 3.64 mm
In-plane resolution	34 µm/m

$$\begin{bmatrix}\sigma_x\\ \sigma_y\\ \sigma_s\end{bmatrix}=\begin{bmatrix}Q_{yy} & \nu Q_{yy} & 0\\ \nu Q_{yy} & Q_{yy} & 0\\ 0 & 0 & \dfrac{1-\nu}{2}Q_{yy}\end{bmatrix}\begin{bmatrix}\varepsilon_x\\ \varepsilon_y\\ \varepsilon_{xy}\end{bmatrix} \tag{2}$$

Note that $Q_{xy} = \nu Q_{yy}$ for a linear elastic isotropic material.

We followed the convention in cellulose materials to report mechanical properties in stress/density (specific) units, here listed as $km^2\,s^{-2}$. In practice, this can be accomplished by avoiding a contacting thickness measurement, which is challenging due to compressibility, and was avoided here by using a non-contacting laser measurement. By using stress units as force/width, mechanical properties like stiffness and strength can be recorded in specific units by dividing them by grammage. Specific units provide a common basis when comparing properties across paper and paperboard grades. For homogeneous materials, $[Q]$ is constant and, when using Equation (2) in Equation (1), can be moved outside the integral. For this work, stiffnesses vary spatially, i.e., both $Q_{yy} = Q_{yy}(x, y)$ and $\nu = \nu(x, y)$, and they remain inside the integral, except where stated otherwise.

4.1 Fourier virtual fields method

FVFM was developed by Nguyen et al. (2014) to examine 2D stiffness distribution, and Considine et al. (2017) used this methodology for examination of heterogeneous paperboard stiffnesses, using the same geometry employed here; a condensed description follows. As in Nguyen et al., we assumed a spatially varying Q_{yy} represented as

$$\begin{aligned}Q_{yy}(x,y) &= \sum_{m=0}^{N}\sum_{n=-N}^{N} a_{m,n}\cos 2\pi\left(\frac{mx}{L_x}+\frac{ny}{L_y}\right)\\ &\quad+\sum_{m=0}^{N}\sum_{\substack{n=-N\\ m+|n|\neq 0}}^{N} b_{m,n}\sin 2\pi\left(\frac{mx}{L_x}+\frac{ny}{L_y}\right)\end{aligned} \tag{3}$$

where:

x, y	:	spatial coordinates in x-, y-directions
L_x, L_y	:	Specimen dimensions in x-, y-directions, 44 mm and 140 mm respectively
$a_{m,n}, b_{m,n}$	:	Fourier coefficients of the series
m, n	:	Spatial frequency components
N	:	Maximum values of indices

As in earlier work, u_i^* were unit amplitude sine/cosine waves with the identical frequencies to those for $Q_{yy}(x, y)$ in Equation (3) and ν is assumed to be constant throughout the specimen. Using a constant ν is needed for the Fourier analysis because the unit amplitude sine/cosine frequencies were used to identify $Q_{yy}(x, y)$. Earlier work (Considine et al. 2017) showed that error associated with assuming a constant ν was small because ν is orders of magnitude smaller than Q_{yy}.

Two additional factors were incorporated in the FVFM analysis. To this point, the units for Q_{yy} were force/length. First, conversion to specific stiffness units was accomplished by dividing Q_{yy} by mean grammage. Second, to examine the effect of physical properties, grammage, thickness, and apparent density, we performed additional identifications by weighting the strains by local grammage or local thickness or local apparent density.

$$\begin{aligned}\mathcal{N}\int_S Q_{yy}\mathcal{W}\Bigg[&\left(\varepsilon_x\varepsilon_x^*+\varepsilon_y\varepsilon_y^*+\frac{1}{2}\varepsilon_{xy}\varepsilon_{xy}^*\right)\\ &+\nu\left(\varepsilon_x\varepsilon_y^*+\varepsilon_y\varepsilon_x^*-\frac{1}{2}\varepsilon_{xy}\varepsilon_{xy}^*\right)\Bigg]dS=\int_l T_y u_y^*\,dl\end{aligned} \tag{4}$$

where $\mathcal{N}$ is a normalization factor and $\mathcal{W}$ is a weighting factor. Four different FVFM analyses were performed using different combinations of $\mathcal{N}$ and $\mathcal{W}$ and are listed in Table 3; the $\mathcal{S}^k$ column will be introduced in the next section and was used for the FEMU analyses. The combination of $\mathcal{N} = \overline{g}$, where $\overline{g}$ is mean grammage, and $\mathcal{W} = 1$ assumes that the variation of Q_{yy} best described without incorporating variations of physical properties. The other analyses shown

Table 3: Types of heterogeneity considered in this work. $\varepsilon_y(x, y)$ is local strain in load direction; $t(x, y)$ is local thickness; $g(x, y)$ is local grammage; $\rho(x, y)$ is local apparent density; $\varepsilon_{VM}(x, y)$ is the local von Mises strain. $\mathcal{N}$, $\mathcal{W}$, and S^k are used in Equation (6). $\mathcal{N}$ is a normalizing constant; $\mathcal{W}$ is a weight term; S^k division refers to the manner the material was segmented for FEMU.

Analysis	$\mathcal{N}$	$\mathcal{W}$	S^k division
FVFM	$\overline{g}$	1	N/A
	$\overline{\rho}$	$t(x, y)$	N/A
	1	$g(x, y)$	N/A
	$\overline{t}$	$\rho(x, y)$	N/A
FEMU	$\overline{g}$	1	$\varepsilon_y(x, y)$
	$\overline{\rho}$	$t(x, y)$	$\varepsilon_y(x, y) \cdot t(x, y)$
	1	$g(x, y)$	$\varepsilon_y(x, y) \cdot g(x, y)$
	$\overline{t}$	$\rho(x, y)$	$\varepsilon_y(x, y) \cdot \rho(x, y)$
	$\overline{g}$	1	$\varepsilon_{VM}(x, y)$
	$\overline{g}$	1	$t(x, y)$
	$\overline{g}$	1	$g(x, y)$
	$\overline{g}$	1	$\rho(x, y)$

in the table examine the individual contributions of thickness, grammage and apparent density variations. Using Equation (3) in Equation (4) the solution is performed in the spatial frequency domain by Fourier analysis.

The u_y^* in Equation (1) are kinematically admissible virtual displacements that operate as weighting functions. $\mathcal{W}$ acts directly on the ε_{ij}^*, that are derived from the u_y^*, by modifying them to include spatial variation of the property that $\mathcal{W}$ represents in a particular analysis.

4.2 Finite element model – updating

FEMU is a type of VFM (Avril and Pierron 2007) that iteratively changes the constitutive parameters in an FE model to match behavior of an experiment with the same geometry, boundary and load conditions. The FE displacement field is compared with the full-field experimental displacements. Using a cost function that relates the differences between the displacement fields with respect to input constitutive parameters, a new set of parameters is created for the FE model. The constitutive parameters are iteratively updated until the difference between the displacement fields is minimized. Here, the constitutive parameters, Q_{yy} and ν are set for each individual element.

Our cost function was based on strains instead of displacements. Our rationale for this change was based on two considerations. First, high-strain regions are failure precursors, and we planned to use strain levels as one method for material segmentation. Second, we wanted to use common inputs for all the inverse methodologies. *SolidsPy* (Gómez and Guarín-Zapata 2018), Python-based 2D finite element analysis code for linear elastic models, was used with 4-node linear quadrilateral elements whose centers coincided with the DIC facets, i.e., there was a one-to-one correspondence between finite elements and DIC facets. Corresponding to information in Table 2, elements were 0.75 mm on each side. Constitutive parameters were assigned to each element based on a material segmentation decision, which will be described in Section 4.4.

As we did with FVFM, we incorporated $\mathcal{N}$ and $\mathcal{W}$ as normalizing and weighting terms, respectively. Whereas FVFM used a function to describe Q_{yy} variation (Equation (3)), with FEMU Q_{yy} and ν can be assigned for each element. In practice, the number of possible Q's and ν's needs to be significantly less than the number of elements, to create an underdetermined system. To incorporate constitutive parameter variation, we rewrite Equation (1) to include discrete heterogeneity by dividing the 2-D domain S into p subdomains with

$$S = \sum_{k=1}^{p} S^k \tag{5}$$

Here we specified p = 250; that is, 250 divisions of the specimen were made to examine heterogeneity. For FEMU, the possible $\mathcal{N}$, $\mathcal{W}$, and S^k are listed in Table 3. The criteria used to segment S are described in Section 4.4. Magnitude of p is limited by the amount of DIC data and the condition of a matrix that needs to be inverted in the FEMU analysis. Besides these considerations, our selection of p was also chosen to reduce analysis time. Based on our DIC data density, the maximum p was near 500.

Using Equation (2) in Equation (1) with only a force in the y-direction, PVW is written as

$$\mathcal{N} \sum_{k=1}^{p} \int_{S^k} Q_{yy}^k \mathcal{W} \left[\left(\varepsilon_x \varepsilon_x^* + \varepsilon_y \varepsilon_y^* + \frac{1}{2} \varepsilon_{xy} \varepsilon_{xy}^* \right) + \nu^k \left(\varepsilon_x \varepsilon_y^* + \varepsilon_y \varepsilon_x^* - \frac{1}{2} \varepsilon_{xy} \varepsilon_{xy}^* \right) \right] dS^k = \int_l T_y u_y^* \, dl \tag{6}$$

Equation (6) was not used explicity in the FEMU; rather it is a representation of the VFM that could have been used for identification. FEMU and VFM are very similar, and we show this equation to demonstrate the inverse procedure incorporated here. Strains were determined from DIC analysis. The identifications were performed in Python (Python 3.7, www.python.org).

4.3 Alignment of data

The pattern printed on the specimen was a convenient tool to align thickness, grammage, and strain data. During the TLP thickness testing, the four corners of the tested region were identified by photographing a laser spot with respect to the printed pattern. Photoshop® (Adobe Inc.) was used to align the local thickness map with an optical image of the printed side of the sample to a resolution of ±20 μm. Using the same software, calibrated grammage maps were superimposed and resized to match the geometry of the dog bone to the same spatial resolution. Map alignment was checked by toggling between thickness and grammage maps, which in all cases showed common features.

After aligning the thickness and grammage data, those data sets were aligned with the first reference image, an averaged image from the first 10 N hold period, using **registrationEstimator** (The MathWorks Inc. 2020). This registration identified the edge pixels of the thickness and grammage data that corresponded to the reference image of the DIC analysis. The spatial density for thickness and grammage data was greater than that of the DIC data. One-to-one correspondence of each set of data was accomplished using the function **griddata** (Python v3.7).

4.4 Material segmentation

Based on work by other researchers, grammage, thickness, density, and different types of strain were used to examine stiffness heterogeneity created by their variation. Twelve different heterogeneous examinations were performed for each material at each load cycle; those examinations are listed in Table 3. The FVFM formulation, Equations (1) and (3), has no direct method of examining the effect of thickness, grammage, or density variations so $\mathcal{W}$ was used to weight the DIC subset strains by one of the heterogeneous variables.

For FEMU, each analysis divided the specimen into 250 segments (p = 250 in Equation (6)) of approximately 44 elements, which could be slightly more or less depending on the common inspection region for the thickness and grammage tests. Each of the 44 elements was assigned the same material properties and did not need to be contiguous. Those material properties were based on the type of heterogeneity in Table 3. Treating the material segments as bins in a histogram analysis, near the center of the chosen distribution, the bin sizes (minimums and maximums) would be close to each other, but farther apart as the values went to each tail. In this work, division by $\varepsilon_{\mathrm{VM}}$, von Mises strain, did not produce the best equilibrium for the specimens but was included because some yield criteria incorporate von Mises stress (e.g. (Ostoja-Starzewski and Castro 2003)).

For each material, 72 different local stiffness identifications were performed, twelve different material analyses as given by Table 3 for five load cycles and the final image before failure.

4.5 Determination of local equilibrium

Devivier et al. (2013) used another VFM formulation to detect damage in composite materials by examination of local equilibrium. Discrepancies in local equilibrium are 'equilibrium gaps' (EG) and can be used to locate boundaries of regions that are not in equilibrium with each other when material homogeneity is assumed. We extend this work to incorporate heterogeneous stiffness by assuming a spatially-varying Q_{yy}.

Using Equation (2) in Equation (1), the PVM can be rewritten as:

$$\int_{S'} Q_{yy}\left[\left(\varepsilon_x\varepsilon_x^* + \varepsilon_y\varepsilon_y^* + \frac{1}{2}\varepsilon_{xy}\varepsilon_{xy}^*\right) + \nu\left(\varepsilon_x\varepsilon_y^* + \varepsilon_y\varepsilon_x^* - \frac{1}{2}\varepsilon_{xy}\varepsilon_{xy}^*\right)\right]dS' - \int_{\partial S} T_i u_i^*\, dl = 0 \tag{7}$$

Equation (7) describes the equilibrium of a region S', where S' is a portion of a larger region, S. If both Q_{yy} and ν are known, either from FVFM or FEMU, and u_i^* are admissible, then summation of the integrals should be zero; a non-zero result is an equilibrium gap. Because no external forces are applied, the final term containing $\overline{T}_i$ is 0. The virtual mesh used for EG analysis was a 2 virtual element by 2 virtual element mesh, and each element was a 4-node linear quadrilateral, which was rastered over the entire specimen. The size of each element is user defined. Here, each virtual element contained 9 DIC data points (3 points × 3 points), and the inspection window was rastered by a single DIC row or column. All virtual degrees of freedom for nodes on the edge of the inspection window were set to zero, which eliminated all work of external forces on the window boundary. The single internal virtual node, the one common to all elements, was subject to a 45° displacement fixed at $|u^*| = 1$. Equation (7) was discretized using summations, and EG was the sum of the internal virtual work over 36 points. EG is not defined at the borders of the specimen within 3 DIC facets because EG has no interpretation when one of the four elements contains no data in a row or column.

We define the quality of the local equilibrium for the entire specimen as:

$$V_0 = \sqrt{\frac{\sum_{i=1}^{N} EG_i^2}{N}} \tag{8}$$

where:
EG_i = each EG at every location in the specimen
N = total number of values of EG for the entire specimen

V_0 is the square root of the variance with a 0 mean value. Ideally, μ(EG) = 0 (mean), and R(EG) = 0 (range). V_0 is a composite value, considering both nonzero means and ranges.

Using the EG for each cycle for those analyses and types listed in Table 3, the smallest V_0 for each of those combinations will determine what type of heterogeneity provided the equilibrium nearest to 0. That smallest value was denoted V_0^{I}, where I denotes inverse method. The EG for the homogeneous material assumption was calculated using Q_{yy}^{H}, which is single-valued and given by:

$$Q_{yy}^{\mathrm{H}} = F \Big/ (w \cdot \overline{\varepsilon_y} \cdot \overline{g}) \tag{9}$$

F: applied force
w: specimen width
$\overline{\varepsilon_y}$: mean DIC axial strain
$\overline{g}$: mean grammage

Similarly, the EG for the 'local' assumption was calculated using $Q_{yy}^{\mathrm{L}}(x,y)$, an array of values given by:

$$Q_{yy}^{\mathrm{L}}(x,y) = F \Big/ (w \cdot \varepsilon_y(x,y) \cdot \overline{g}) \tag{10}$$

F: applied force
w: specimen width
$\varepsilon_y(x, y)$: DIC axial strain at location (x, y)
$\overline{g}$: mean grammage

4.6 Data analysis

As stated earlier, DIC analysis was performed MatchID v2022.2.1; grammage, thickness, density and registration of those data with DIC was performed in Matlab R2023a® and saved as a dataset. The inverse method analyses were performed with script written with Python 3.7 and performed with an Windows 10 system, with 2.10 GHz Intel Xeon 4216 CPU and 96 GB RAM. The 72 inverse analyses (12 inverse method analyses × 6 cycles) took approximately 16 h. Most of this time was for FEMU analyses; a single FVFM analysis would take less than 30 s.

5 Results and discussion

Heterogeneity analysis of twelve difference specimens of commercially produced paper and paperboard are presented as representative of a larger study. These specimens were selected from the larger group based on two criteria: (1) the initial failure zone was away from the edge of the specimen, and (2) the local stiffness was well-identified, as determined by the smallest V_0^{I} of the 60 different heterogeneous linear elastic stiffness identifications performed.

5.1 Grammage, thickness, density

Table 1 provides a list of materials used in this work, their types, and information about their grammage, thickness, and density. The coefficient of variation (COV) describes the spread in the distribution of a particular property, normalized by its mean. Kurtosis, K, is a measure of the prevalence of outliers of a distribution. The greater K, the greater the prevalence of outliers. For a normal (Gaussian) distribution, $K = 3$, so if $K < 3$, outliers are less common, and if $K > 3$, outliers are more common, than found in the normal distribution. Three of the materials, G, I, and J, exhibited high grammage kurtosis ($K(g)$), indicating they had large spread in local grammage. None of the materials exhibited high kurtosis in thickness, indicating greater uniformity in thickness. Only Material G exhibited excess kurtosis in density.

Skewness, S, is a measure of the symmetry of the distribution. Generally, an absolute value of S less than 0.5 indicates a nearly symmetric distribution. A value of $S > 1$ indicates the distribution is 'skewed right,' that is, it tends to exhibit a heavier right tail than left. Similarly, $S < -1$ indicates the distribution is 'skewed left.' For materials G, I, and J, grammage was significantly right-skewed, a condition more akin to a gamma or Weibull distribution than the normal. The remaining distributions for grammage and all for thickness exhibited near-symmetry. Only Material G exhibited significant right skew in density, and only Material T exhibited significant left skew in density.

The Anderson-Darling test for normality indicated that none of the distributions for g or t was normally distributed. However, a number of these datasets can fit well to a mixture of two distributions, such as a gamma or a Weibull. For example, a 4-parameter bivariate distribution given by the following density provides reasonable fitment for both the g and t observations over most of the specimens:

$$f(x) = \theta \cdot \frac{x^{\alpha-1} e^{x/\beta}}{\Gamma(\alpha)\beta^{\alpha}} + (1-\theta) \cdot \frac{k}{\lambda}\left(\frac{x}{\lambda}\right)^{k-1} e^{-(x/\lambda)^k} \cdot I\{x \geq 0\}$$

where $\theta \in (0, 1)$ and the constraint, $\alpha\beta = \lambda\Gamma(1 + k^{-1})$ holds. This, in essence, suggests that grammage and thickness of the observed specimens may be 'mostly' modeled by a gamma distribution, excepting only a small proportion of the observations that deviate greatly from typical values. For those values, a Weibull distribution with the same mean, but a much larger COV could apply.

Grammage contours are shown in Figure 5, normalized by their individual mean grammage. The most uniform materials were F and W; the ones with the most heterogeneous grammage were G and I. A histogram comparing the distributions of normalized grammage for Materials W and G is shown in Figure 6, providing another visualization of the greater grammage homogeneity of Material W compared with Material G.

Thickness contours are shown in Figure 7, normalized by their individual mean thicknesses. The most uniform materials were W, E and F; the ones with the most heterogeneous thickness were G and S. A histogram comparing the distributions of normalized thickness for Materials E and

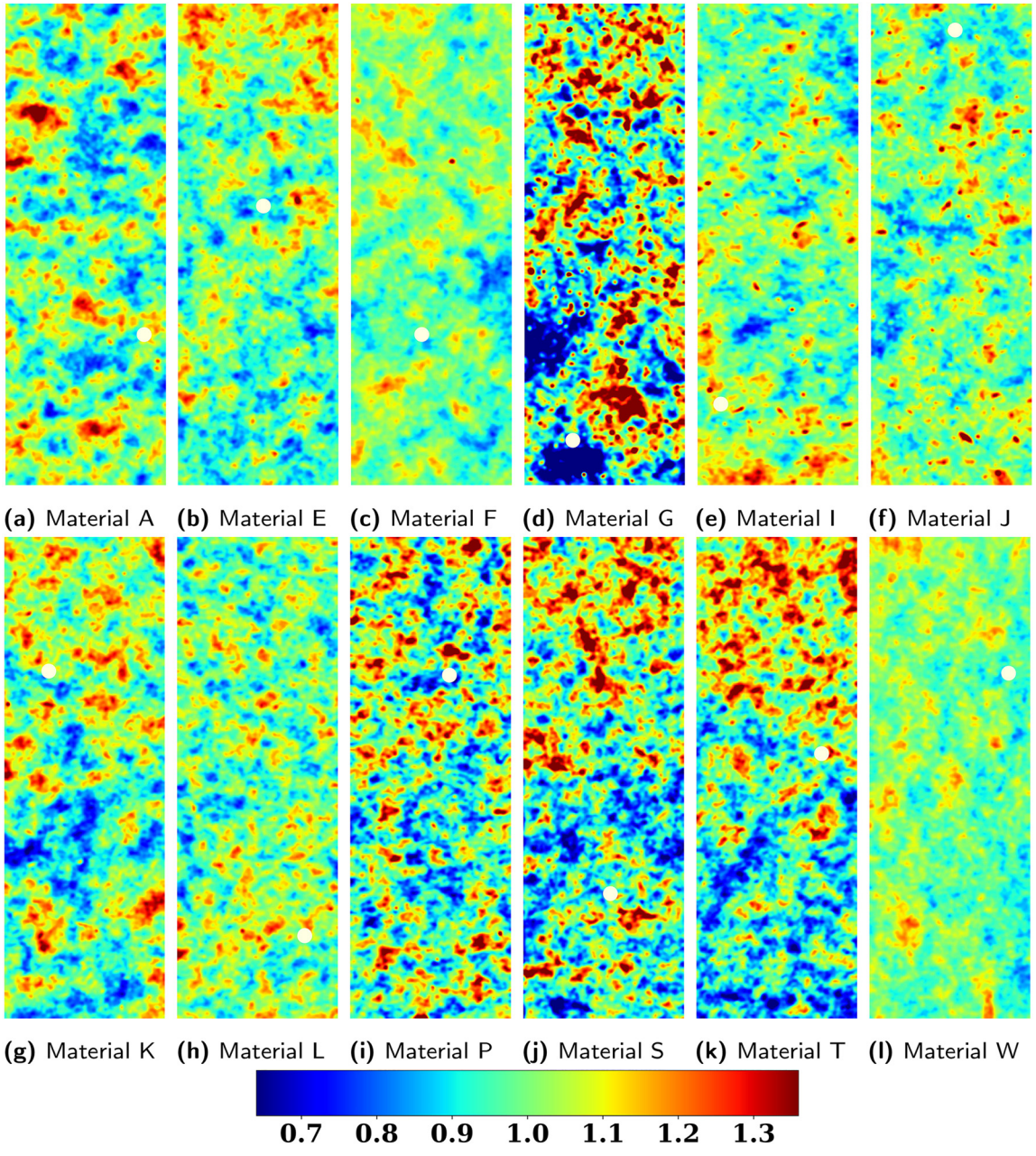

Figure 5: Grammage contours for these materials, normalized by their individual mean grammage. Maps are nominally 44 mm wide and 140 mm high. White circles denote inital failure location.

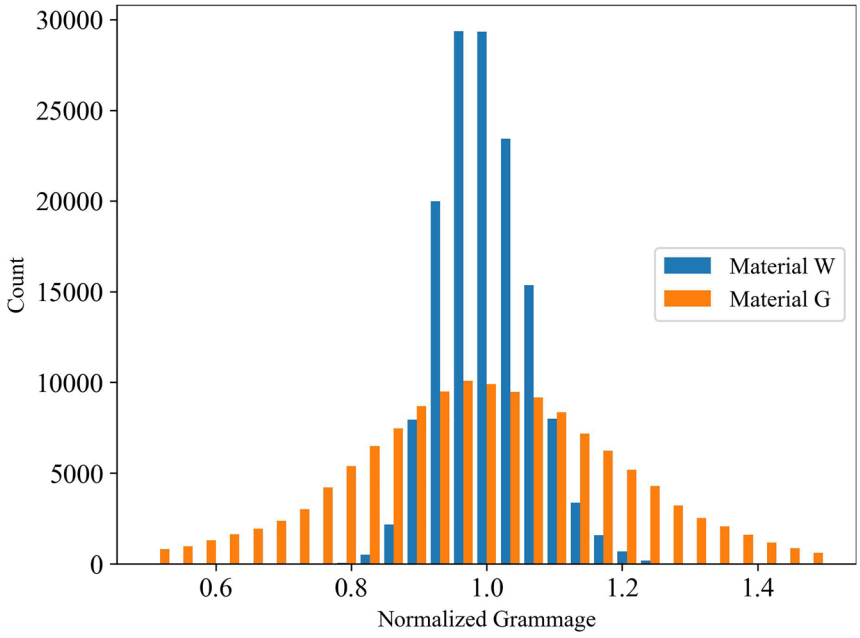

Figure 6: Histograms of normalized grammage for Materials W and G.

S is shown in Figure 8, providing another visualization of the greater thickness homogeneity of Material E as compared to Material S.

Density contours are given in Figure 9, normalized by their individual mean densities. A few of the materials, G, P, and S, had very localized high-density regions. Stiffness identification around those regions, where high density regions are surrounded by low density regions, are very challenging, because the DIC will tend to blur high and low strains within each facet.

Material T density (Figure 9k) shows a dramatic vertical density variation. This variation can be seen in Figure 5k, but to a lesser extent and the low thickness region shown at the top in Figure 7k each combine to produce this large variation. This physical property variation is called a 'streak' in papermaking technology.

The selected materials exhibited a wide range of physical heterogeneity. The failure locations, as denoted by the white circles, will be discussed in Section 5.3.

5.2 Linear elastic stiffness heterogeneity

Materials W and G had the smallest and largest variation, for both grammage and thickness, respectively. Figure 10 shows their strain contours for the particular load cycle that produced the smallest V_0^{I}. Material G specimen showed some regions with $\varepsilon_x > 0$, a negative Poisson region. The range for ε_{xy} for Material W, Figure 10c, is small; the contour demonstrates the good strain resolution for the stereo DIC system with range of ±4× strain resolution.

Previous work (Considine et al. 2017) demonstrated that with careful grip clamping in the test machine that emphasizes specimen alignment, strain heterogeneity was not caused by improper specimen gripping. In that work the specimens were rotated 180°, top-to-bottom, after 5 tensile cycles and then 5 more tensile cycles were performed before testing to failure. The strain heterogeneity remained after pausing and rotating. The presence of mechanical heterogeneity, either by non-uniform ε_x or non-zero ε_{xy}, creates challenges during tensile testing, because the specimen is trying to conform to its lowest energy form, which is likely no longer rectangular. Finally, the use of grip displacement with original grip separation distance as a surrogate for strain measurement creates an imbalance between less heterogeneous and more heterogeneous materials, which requires the use of full-field displacement measurements for accurate stiffness identification.

Table 4 shows some results of the analysis for heterogeneous stiffness identification. The heterogeneity analysis with the smallest V_0^{I} is shown. Note that the analysis depended on both analysis types, FVFM or FEMU, and if FEMU, one of the eight material segmentations. Cycle 1 did not produce the best equilibrium for any material, which was expected because the load for Cycle 1 was near the nonlinear regime. Otherwise, each cycle possibility, from 2-5, was represented. Q_{50} denotes the 50th percentile for the stiffness, which is given in specific stiffness units. COV(Q) is the coefficient of variation for Q; note use of COV assumes a normal data distribution, which is valid only for a few of the materials. Q_T refers to initial stiffness of final portion of the test schedule as shown in Figures 3 and 4.

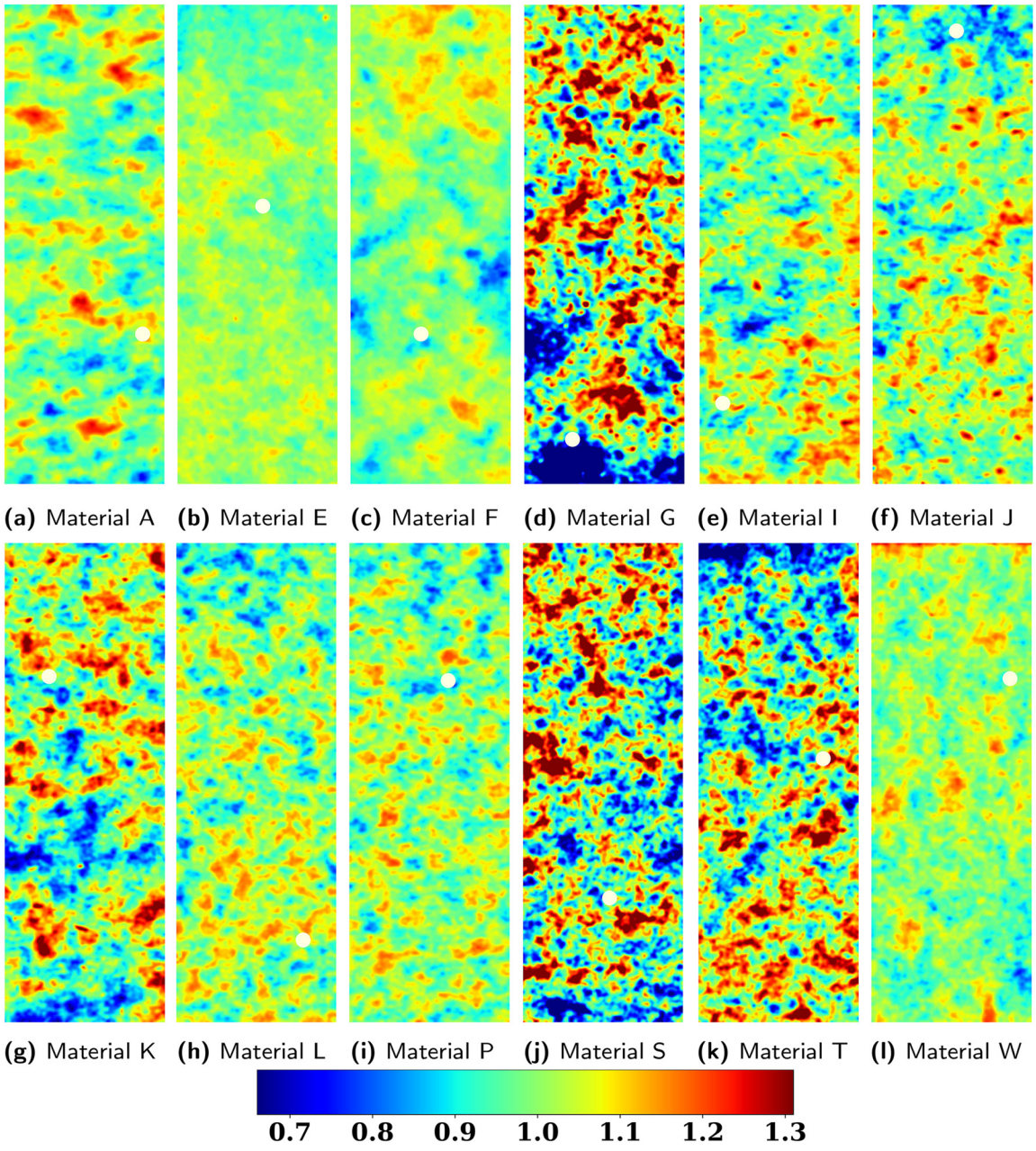

Figure 7: Thickness contours for these materials, normalized by their individual mean thickness. White circles denote initial failure location.

The initial stiffness was calculated using a hyperbolic tangent model given by

$$L = C_1 \tanh\left[C_2\left(\overline{\varepsilon}_y - C_4\right)\right] + C_3\left(\overline{\varepsilon}_y - C_4\right) \tag{11}$$

where L is applied load/width, $\overline{\varepsilon}_y$ is mean axial strain and C_i are constants to be fit.

The Q_T, the initial stiffness, is given by:

$$Q_T = (C_1 \cdot C_2 + C_3)\big/\overline{g}\big/(1-\overline{\nu}^2) \tag{12}$$

where $\overline{\nu}$ is the mean Poisson ratio determined from DIC and $\overline{g}$ is the mean grammage.

Q_T is expected to have larger magnitude than Q_{50} because Q_T is a tangent stiffness of the initial portion ($\overline{\varepsilon}_y = 0$) of the $\sigma - \varepsilon$ curve, whereas Q_{50} is a secant modulus corresponding to the slope between two load levels. Only Material T had $Q_{50} > Q_T$. We have no explanation for this anomaly other than some damage may have occurred during the first five cycles.

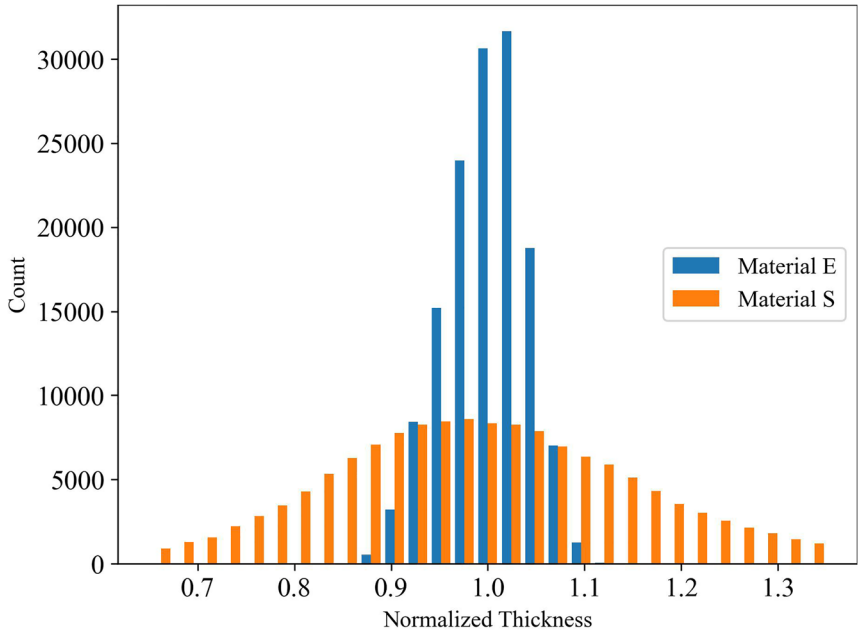

Figure 8: Histograms of normalized thickness for Materials E and S.

None of the materials had their best $Q_{yy}(x, y)$ identification influenced by grammage, i.e., neither $\mathcal{W}$ nor S^k used g (grammage) in the identification. Recall $\mathcal{N}$ is a normalizing term to create the proper units for specific stiffness. Of the twelve materials, six had local stiffness dominated by density (ρ or $\varepsilon_y \rho$) (Materials I, J, L, P, T, and W), five had local stiffness dominated by thickness (t) (Materials E, F, G, K, and S), and Material A had local stiffness not dominated by either of the three physical properties. These results indicated that local thickness measurement, needed for t and ρ, was critical for heterogeneous stiffness identification. With current technology, this moves the process described here from the plant to the laboratory because local thickness measurement is a time-consuming process requiring non-standard equipment. For Material A, its heterogeneity may be caused by other factors or combinations of other factors, e.g., residual stresses, local fiber misalignment.

The FEMU provided the best Q identification in 5 of the 12 materials. Two of those materials, L and T, had local stiffness best identified with material division by ρ and combination of ρ and $\varepsilon_y \rho$, respectively. Table 5 gives the best five inverse analyses (out of 60 possible) for each of these materials, showing that although use of ρ produced the smallest V_0^{I}, for Material L, t also produced a good equilibrium. For Material L, this behavior could be anticipated given the relationship between g and t shown in Figure 11a. However, Material T did not have a strong relationship between g and t, as indicated in Figure 11b.

The improvement factor, $\mathcal{I}$, is a metric assessing the magnitude of the local equilibrium improvement of the inverse methodology, and is given by:

$$\mathcal{I} = \left(1 - V_0^{\mathrm{I}} / V_0^{\mathrm{H}}\right) \times 100 \tag{13}$$

where:

V_0^{I} = the smallest V_0 for that specimen for the 60 different inverse analyses

V_0^{H} = is the homogeneous variance determined by using Equation (9), Q^{H}, the homogeneous stiffness

Table 6 gives V_0^{I}, V_0^{H}, V_0^{L}, and $\mathcal{I}$, using the data from the lowest V_0^{I} for each material. Material L had a 13 % improvement from the homogeneous assumption. The heterogeneous analysis improved the equilibrium of the other eleven materials by at least 20 %. Material K had the greatest improvement at 98 % and had the smallest V_0^{I}, indicating that its identified stiffness produced best local equilibrium. Material W had a 42 % improvement in equilibrium by incorporating heterogeneity based on density (see last row of Table 4). This result was unexpected for Material W because it was presumed to have nearly homogeneous behavior. Considering its density profile, Figure 9l, which had generally lower variations than other materials, the improvement demonstrated that the heterogeneity analyses described here can guide quality enhancement processes.

Material A was the only material whose best local equilibrium did not include grammage, thickness, or apparent density. This material had the highest grammage

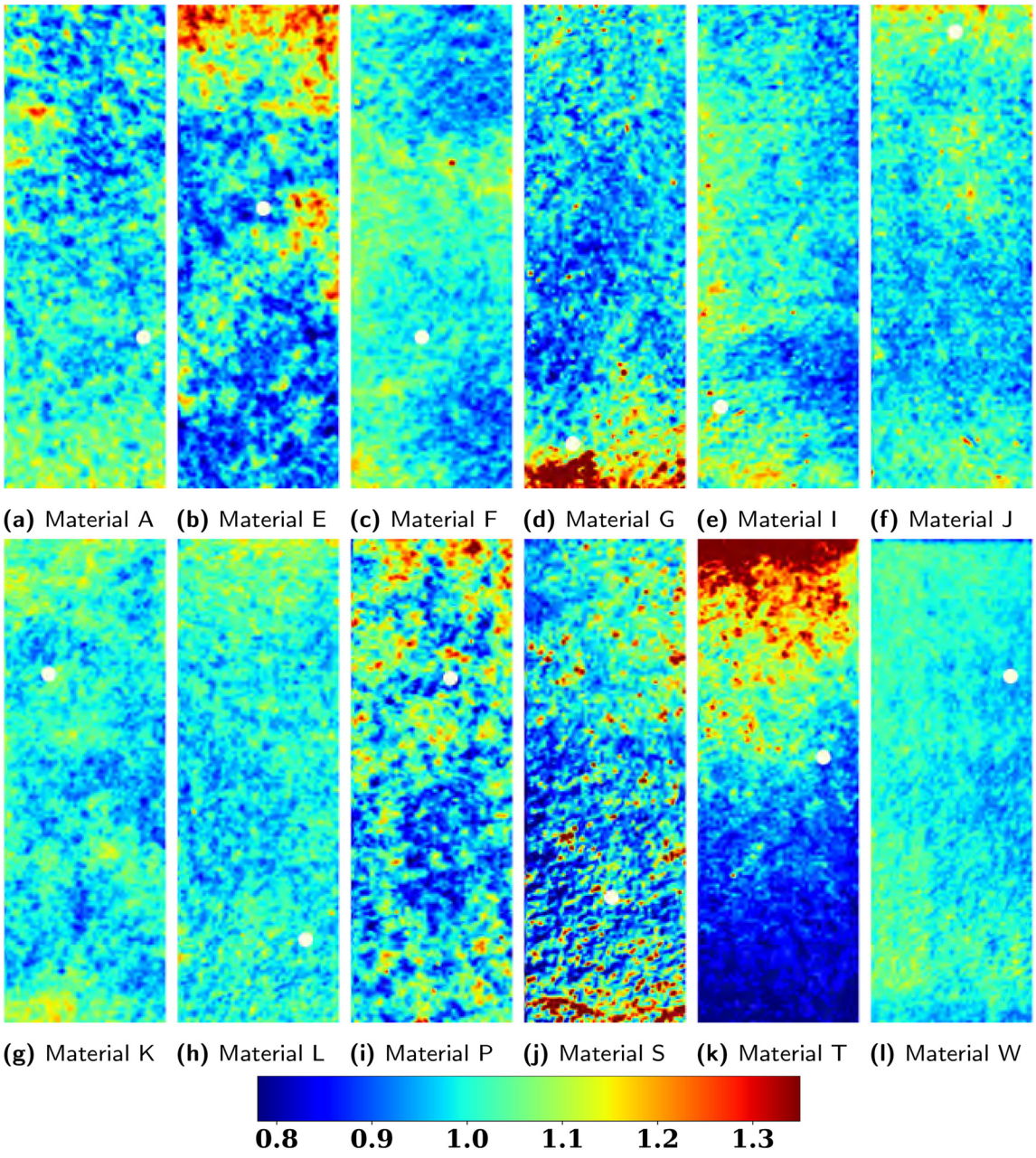

Figure 9: Density contours for these materials, normalized by their individual mean density. White circles denote initial failure location.

(269 g m^{-2}) and was a multi-ply linerboard. Its variations of physical properties was lower, with COV(g) the highest among them at 11 %. Multiple plies can mask differences in properties of individual plies, e.g., a lower grammage region in one ply can be compensated by higher grammage in another ply in the same region and vice versa. Additionally, this material had the greatest thickness, 314 µm, and the assumption of uniform strain through the thickness may not be valid; this could be examined by using another stereo DIC system to interrogate the back side of the specimen, but this was not employed here. Analysis of additional specimens of this material may provide supplementary information to guide future efforts.

Figure 12 shows the Q contour maps for the type and analysis with the smallest V_0^{I} as given in Table 4. Materials G, I, J and K had significant 'ringing' near their vertical edges. Ringing is an artifact of the Fourier analysis that occurs near edges and is associated with band limitations. Here, the

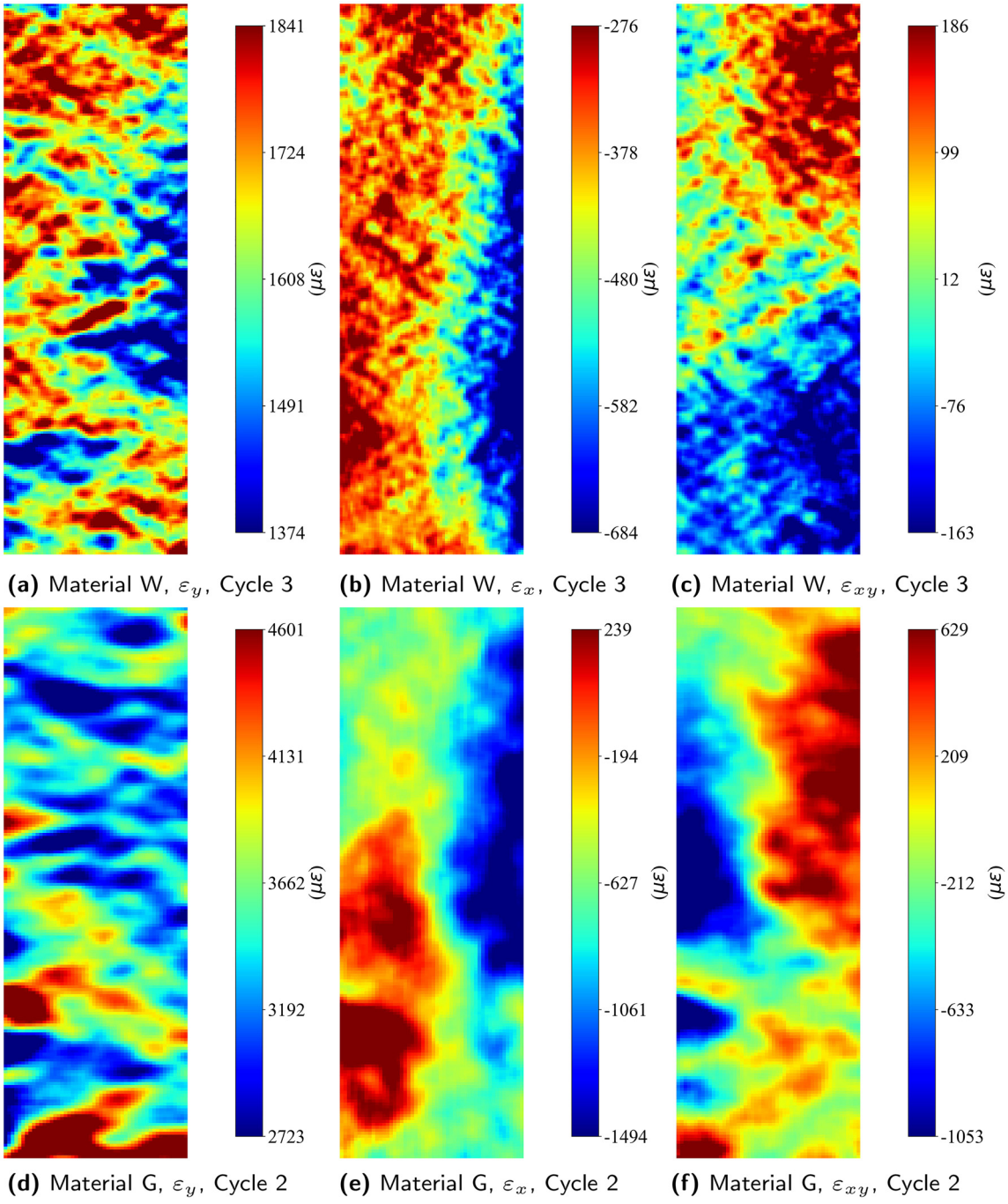

Figure 10: Strain contours for Materials W and G, the materials with the smallest and largest thickness and thickness variations, respectively.

magnitude of N in Equation (3) is limited by specimen width, which is much smaller than its length. N was maximized according to data density after alignment and varied from 11-13; N = 11 produces 540 Fourier coefficients in Equation (3). Our selection of specimen geometry was designed to reduce the ringing effect, by using a wider specimen than normal, but not so wide as to induce tensile buckling (wrinkling) in the linear elastic regime, and to be applicable to several paper grades. Therefore, ringing does not represent actual $\underline{Q}$ variation, but rather a fit to Fourier coefficients. Tensile buckling occurred in several of the materials prior to failure in the final portion of the tensile test.

Materials E and W had the smallest COV(Q)s, and their uniformity is apparent in their contours (Figure 12b–l).

Table 4: Results from this work. Q_{50} indicates 50th percentile of Q. K and S denote Fisher kurtosis and skewness, respectively, for the Q distribution. Q_T refers to the initial stiffness of the final portion of the test.

Material	Analysis	$\mathcal{N}$	$\mathcal{W}$	S^k	Cycle	Q_{50} (km^2 s^{-2})	Q_T (km^2 s^{-2})	COV(Q) (%)	K	S
A	FVFM	$\overline{g}$	1	N/A	3	4.34	4.39	58	1.3	−1.0
E	FEMU	$\overline{g}$	1	t	4	3.27	4.93	6	−0.2	−0.1
F	FVFM	$\overline{\rho}$	t	N/A	3	3.60	4.39	49	10.6	2.7
G	FVFM	$\overline{\rho}$	t	N/A	2	2.96	4.25	104	5.3	1.1
I	FVFM	$\overline{t}$	ρ	N/A	3	2.73	3.42	86	14.9	2.4
J	FVFM	$\overline{t}$	ρ	N/A	5	2.68	3.29	82	19.1	3.1
K	FVFM	$\overline{\rho}$	t	N/A	3	3.78	4.49	109	20.4	1.9
L	FEMU	$\overline{t}$	ρ	$\varepsilon_y \cdot \rho$	2	2.60	2.80	16	1.0	0.6
P	FVFM	$\overline{t}$	ρ	N/A	4	2.20	2.60	24	18.3	3.1
S	FEMU	$\overline{\rho}$	t	$\varepsilon_y \cdot t$	5	4.01	5.61	58	83.6	7.5
T	FEMU	$\overline{t}$	ρ	$\varepsilon_y \cdot \rho$	3	6.35	5.78	24	0.0	0.5
W	FEMU	$\overline{g}$	1	ρ	3	1.45	2.32	7	14.3	2.1

Table 5: Comparison of analysis for Materials L and T, whose Q identification depended on physical properties. The inverse analysis for all data in this table was FEMU and represents results with the lowest five V_0^{I} out of the 60 possible results, sorted by V_0^{I}.

Material	Analysis	$\mathcal{N}$	$\mathcal{W}$	S^k	Cycle	Q_{50}	V_0^{I}
L	FEMU	$\overline{t}$	ρ	$\varepsilon_y \cdot \rho$	2	2.60	1.483
	FVFM	$\overline{t}$	ρ	N/A	5	2.58	1.551
	FEMU	$\overline{t}$	ρ	$\varepsilon_y \cdot \rho$	4	2.69	1.567
	FEMU	$\overline{g}$	1	t	5	2.61	1.570
	FVFM	$\overline{t}$	ρ	N/A	2	2.55	1.592
T	FEMU	$\overline{t}$	ρ	$\varepsilon_y \cdot \rho$	3	6.35	2.789
	FEMU	$\overline{t}$	ρ	$\varepsilon_y \cdot \rho$	2	6.38	3.189
	FEMU	$\overline{t}$	ρ	$\varepsilon_y \cdot \rho$	4	6.14	3.232
	FEMU	$\overline{t}$	ρ	$\varepsilon_y \cdot \rho$	5	6.41	3.599
	FEMU	$\overline{g}$	1	ρ	4	6.07	4.107

Table 6: Comparison of V_0's for each analysis. Only the smallest V_0^{I} for each material is shown; V_0's have units (km^2 s^{-2}). $\mathcal{I}$ denotes improvement from assumed homogeneity as determined from Equation (13).

Material	V_0^{I}	V_0^{H}	V_0^{L}	$\mathcal{I}$ (%)
A	2.31	3.71	4.63	38
E	2.59	3.23	3.75	20
F	2.37	4.02	3.35	41
G	2.65	4.36	3.99	39
I	1.92	3.33	3.59	42
J	2.05	3.85	4.48	47
K	0.19	11.95	9.14	98
L	1.48	1.70	1.96	13
P	2.12	2.67	2.50	21
S	7.80	11.76	12.53	34
T	2.79	5.24	4.27	47
W	0.80	1.37	1.30	42

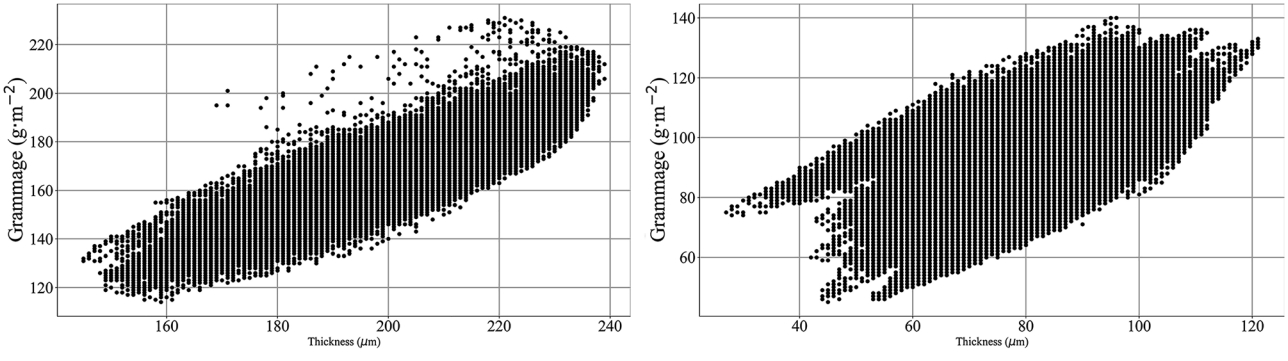

(a) Material L **(b)** Material T

Figure 11: Thickness and grammage relations for materials L and T.

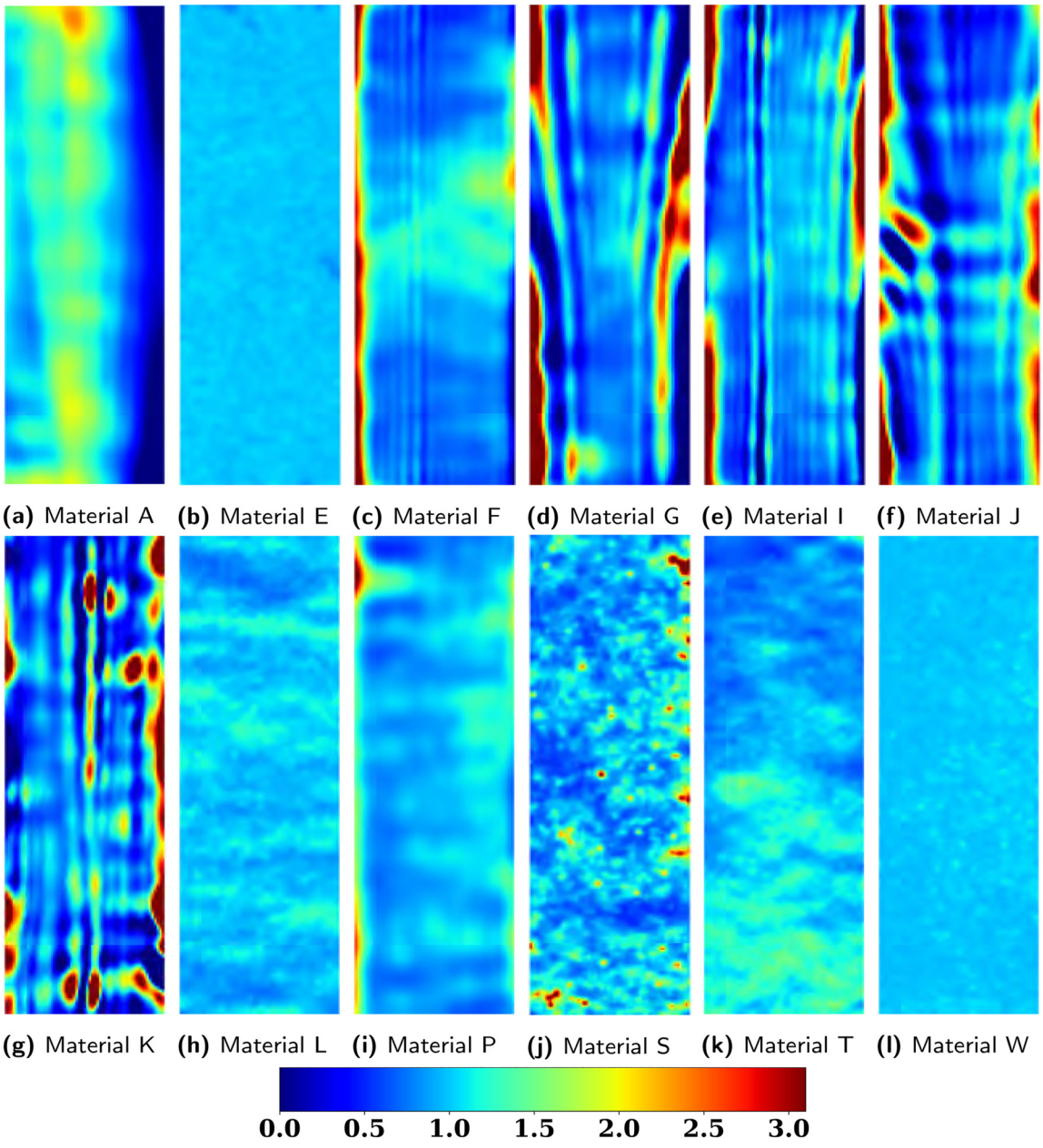

Figure 12: Q contours for these materials, normalized by their individual mean Q. Data was smoothed with Gaussian filter for visualization. 'Ringing' (stripiness) is an artifact the FVFM analysis.

Materials A and S had COV(Q) = 58 %, but their stiffness contours show different kinds of variation. Material A had an almost centrally located stiffness streak, whereas Material S had very localized high stiffness regions. The Q distribution for A was nearly normal, whereas for S the distribution was skewed to high stiffness ($S(Q) = 7.5$) and with several outliers ($K(Q) = 83.6$). Localized high stiffness regions have the potential to be stress concentrators, thereby reducing tensile strength.

Material G had high apparent density (>1000 kg m^{-3}) and a wide distribution for thickness (COV(t) = 20 %, the largest among all materials). Its best Q identification depended on thickness ($\mathcal{W} = t$) and resulted in one of the largest COV(Q)s at 104 %. Strain heterogeneity is shown in Figure 10d, e, and f. Strain ε_y and thickness contour (Figure 7d) show good correspondence.

The data that produced the smallest V_0^{I} for each specimen are shown in Figure 13 and are normalized by their

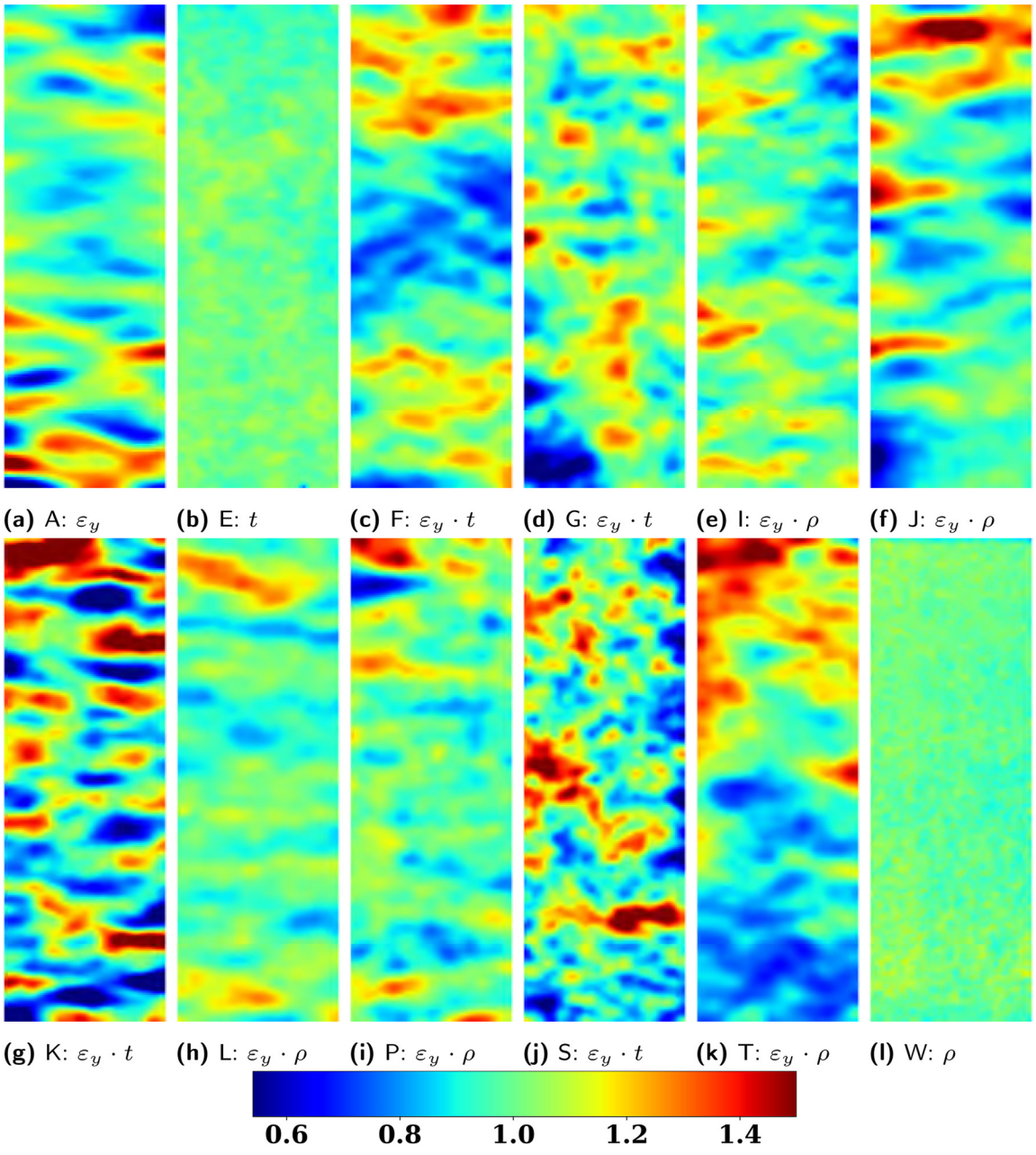

Figure 13: Normalized contours for materials which produced the smallest V_0^I.

respective mean values. Materials E and W were best identified with FEMU and t and ρ segmentation, respectively, each of which have minimal spatial orientation. The other materials had identification controlled by ε_y, and variation was generally controlled by y location. This result provides another reason to choose CD orientation for mechanical testing because the FVFM analysis works best when the dominant variation is in the long dimension of the specimen.

Materials E, L, S, T, and W had their best stiffness identification with FEMU. Except for Material T, these materials tended to have lower variations in their contours in Figure 13. For the materials examined, FVFM worked best on materials with large periodic gradients, and FEMU worked best with smaller gradients. Only a small selection of possible material segmentation choices was used for FEMU. Many other segmentation choices are possible, e.g., combinations of physical properties and ε_{VM}.

Q identification for Material K showed large stiffness gradients and had the lowest V_0^{I}. Materials L and W also had small V_0^{I}, but identification in 'more' homogeneous materials should be straightforward. This methodology demonstrates its flexibility by performing good identification on both 'more' heterogeneous and 'more' homogeneous materials.

Five materials (F, G, I, J, and P) had stiffness heterogeneity related to ε_y multiplied by ρ or t. This result agrees with earlier conclusions (Ostoja-Starzewski and Castro 2003), which suggested the representative volume element (RVE) is approximately 10 × the floc size, that is, the floc tends to control the location and shape of the heterogeneity, as determined by t or ρ high/low regions, and ε_y shows the extent of the effect of the floc.

To this point, we have demonstrated a methodology to identify the elastic stiffness heterogeneity in several paperboards and a filter paper and have associated those identifications with a physical property that produces the best local equilibrium. In one case, for Material A, the best equilibrium was achieved without use of any local physical property, indicating its heterogeneity had a different source. Finally, none of the best identifications incorporated local grammage directly. The next section examines heterogeneous stiffness identification just prior to failure, therefore in the nonlinear regime.

5.3 Nonlinear stiffness heterogeneity and tensile strength

Contours of ε_y for the final image before failure are shown in Figure 14. Each contour has a white circle located at the location of failure initiation. In six of the twelve specimens (Materials A, E, F, G, J, and P) the failure initiated in high strain regions, where ε_y in the failure zone, as given by $\varepsilon_{y(f)}$ in Table 7, was ≥90th percentile. Material K had failure zone $\varepsilon_{y(f)} \ll$ 50th percentile (14 %). In the other materials, it initiated in transition regions, between high and low strain regions. This finding generally agrees with Borudilina et al. (2012), who used high strain regions as failure precursors. Table 8 provides additional information regarding the data that produced that smallest V_0^{I} for each material. In only three of twelve materials, the data that produced the smallest V_0^{I} was the same as for the elastic cyclic portion of the test. For ten of the materials, FEMU provided the best heterogeneous stiffness identification. This outcome agrees with the identification in the elastic regime where materials with large non-periodic gradients employed FEMU for their best equilibrium.

The smallest V_0^{I} results for the nonlinear portion of the test, shown in Table 8, were much larger than those for the linear elastic analysis in Table 6; Table 8 shows the best identification for the entire specimen, with no emphasis on the failure zone. These outcomes are best compared material-by-material, because V_0^{I} is determined by the identified Q and the evaluated DIC strains. For the nonlinear portion, Q's will be much smaller and the ε_i's will be larger, but the magnitude of the Q has a larger influence on V_0^{I}. Therefore, the current methodology should be altered to better identify stiffness in the nonlinear regime, perhaps incorporating behavior as given by Equation (12).

Figure 15 shows an example of the tensile behavior during the final portion of the test for Material K. During the initial portion of the test, the overall mean DIC ε_y and the failure zone (approx 1.75 mm × 1.75 mm) DIC ε_y are similar. Only after yield, near 3.5 kN m^{-1}, did the failure zone strain deviate from the overall strain. The linear elastic portion of the test was cycled between 0.23 and 1.82 kN m^{-1}. This behavior, where the failure zone strain was similar to the global mean strain, was similar for all materials. Korteoja et al. (1996) found that large portions of the tensile specimen remained elastic, whereas the smaller areas became plastic and controlled failure.

Failure zone properties are summarized in Table 7. Two materials, G and W, had failure zone physcical properties that could be recognized as failure precursors. Material G had $\mathcal{W} = t$ and its failure zone thickness was in the 1%-tile, i.e., it failed in its thinnest region. Krasnoshlyk et al. (2018) found that a high-density material (>1000 kg m^{-3}) was able to localize fracture. Material W had $S^k = \rho$ and its failure zone density was in the 8th percentile. Other materials did not have strong indication of failure precursors in physical properties.

The remainder of the failure zone analysis relied on forensic, post-failure analysis. The failure zone for Material A was located in a high ε_y gradient region; its identification was influenced by t ($S^k = t$), and the thickness of the zone was in the 90th percentile. Although the failure zone had high grammage and thickness, its density was marginally above the median at the 62nd percentile, so its low Q_c (7th percentile) could be anticipated. This zone seems to have been poorly bonded. While examining newsprint, Moffat et al. (1973) found that calendaring damages high grammage flocs, causing them to become a likely failure location. Unlike paperboards made from kraft pulps, newsprint is composed of mechanical pulp fibers that exhibit weaker interfiber bonding. Hard calendering weakens newsprint by rearranging fibers, especially in high grammage regions that bear the load. Chemical fibers show greater resiliency with less bond breakage.

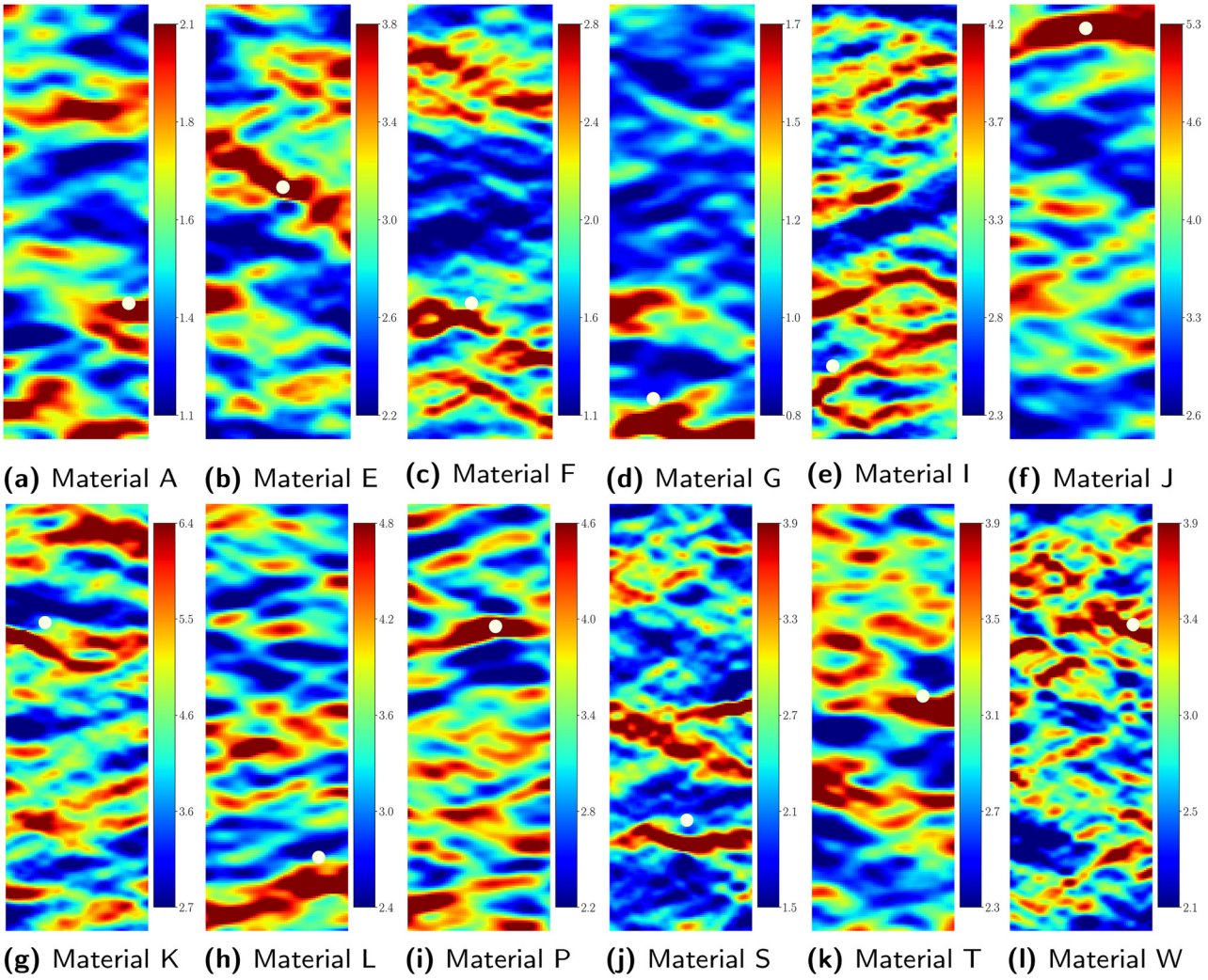

Figure 14: ε_y contours for the final image prior to failure for these materials. Units are (%). White circle denotes initial failure location.

Table 7: Failure zone comparison for specimens. All values are %-tiles for a region approximately 1.75 mm × 1.75 mm around the failure initiation zone. *c* refers to the local value for the particular cycle in Table 3 that had the lowest V_0^1; *f* refers to the local value just prior to failure.

Material	Grammage	Thickness	Density	$\varepsilon_{y(c)}$	$\varepsilon_{y(f)}$	Q_c	Q_f
A	89	90	62	43	99	7	36
E	14	37	20	77	98	24	10
F	25	23	44	72	96	25	35
G	1	1	96	98	98	92	62
I	28	19	77	14	62	99	68
J	38	15	93	77	91	6	12
K	87	90	23	27	14	76	71
L	45	49	43	72	84	54	58
P	32	24	52	88	90	37	19
S	73	87	20	76	38	22	47
T	63	69	51	51	47	51	15
W	9	30	8	2	65	68	48

Table 8: Strength results from this work giving the analysis that produced the smallest V_0^{I} for the final image prior to failure.

Material	Analysis	$\mathcal{N}$	$\mathcal{W}$	S^k	V_0^{I}
A	FEMU	$\bar{g}$	1	t	10.83
E	FEMU	$\bar{t}$	ρ	$\varepsilon_y \cdot \rho$	5.98
F	FEMU	$\bar{g}$	1	t	19.51
G	FVFM	$\bar{\rho}$	t	N/A	4.52
I	FEMU	$\bar{g}$	1	t	16.30
J	FEMU	$\bar{t}$	ρ	$\varepsilon_y \cdot \rho$	7.54
K	FEMU	$\bar{g}$	1	t	28.99
L	FEMU	$\bar{g}$	1	t	10.07
P	FEMU	$\bar{t}$	ρ	$\varepsilon_y \cdot \rho$	11.72
S	FEMU	$\bar{\rho}$	t	$\varepsilon_y \cdot t$	23.33
T	FVFM	$\bar{t}$	ρ	N/A	15.53
W	FEMU	$\bar{g}$	1	ρ	7.25

Four other materials had very high strains in their failure zones, Materials E, F, J, and P, with Materials A and G discussed earlier. None of the physical properties of their failure zones would indicate a failure precursor. Material P did have a failure zone cyclic strain of 88th percentile.

No definitive conclusions can be drawn from failures of the remaining materials, I, K, L, S, and T. Their failure zones are near or in strain gradient regions that appear like regions near low stiffness or high stiffness regions. Low and high stiffness regions, relative to the neighboring material, create complex strain and stress states. Figure 16 shows the shear strain contours just prior to failure, using the same images used to create Figure 14. If these materials were homogeneous, the shear strain would be zero. However, due to heterogeneity, the shear strains are large and vary between large positive (red) and large negative (blue). Fibrous materials have difficulty resisting shear deformations; most structural applications of these materials are designed to avoid shearing behavior. Additionally, the presence of large shear strains provided the information needed to explain the poor equilibrium analysis for these images. In the linear elastic regime, the shear strains were small and had little contribution to the equilibrium. In the nonlinear regime, these shear strains are large and we have incorporated only an isotropic estimate for shear modulus in Equation (2). Identification of local shear stiffness would contribute to development of failure examinations.

We note that the analysis of the specimens prior to failure showed that the elastic and nonlinear behaviors of most of the materials were not the same. This result corresponds with findings by Na and Muhlstein (2019) who found changes in fiber orientation and floc geometry during testing. In the elastic portion of the test, eight materials were best identified with FVFM analysis, but only two materials in the post yield analysis. Furthermore, the quality of the Q identification as determined by V_0^{I} is much lower in the post yield tests. Efforts to improve this identification are part of ongoing work.

Figure 17 shows the same failure location mapped on the Cycle 5 ε_y data, which was in the linear elastic regime. For Materials A, E, F, G, and S, the failure zone was in a high strain region, but only for Materials G and S was it in the highest strain regions. For Materials I, J, L, P, and T, the failure zone was in a high strain gradient region. For

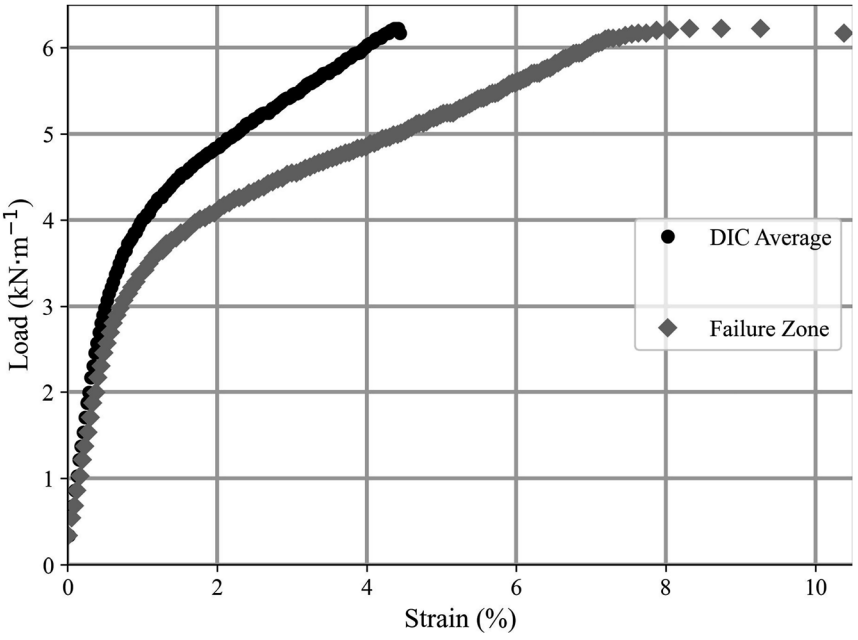

Figure 15: Material K tensile behavior during the last portion of the test. The black symbols are located at the mean DIC ε_y and the gray symbols are located at the mean DIC ε_y for the failure zone.

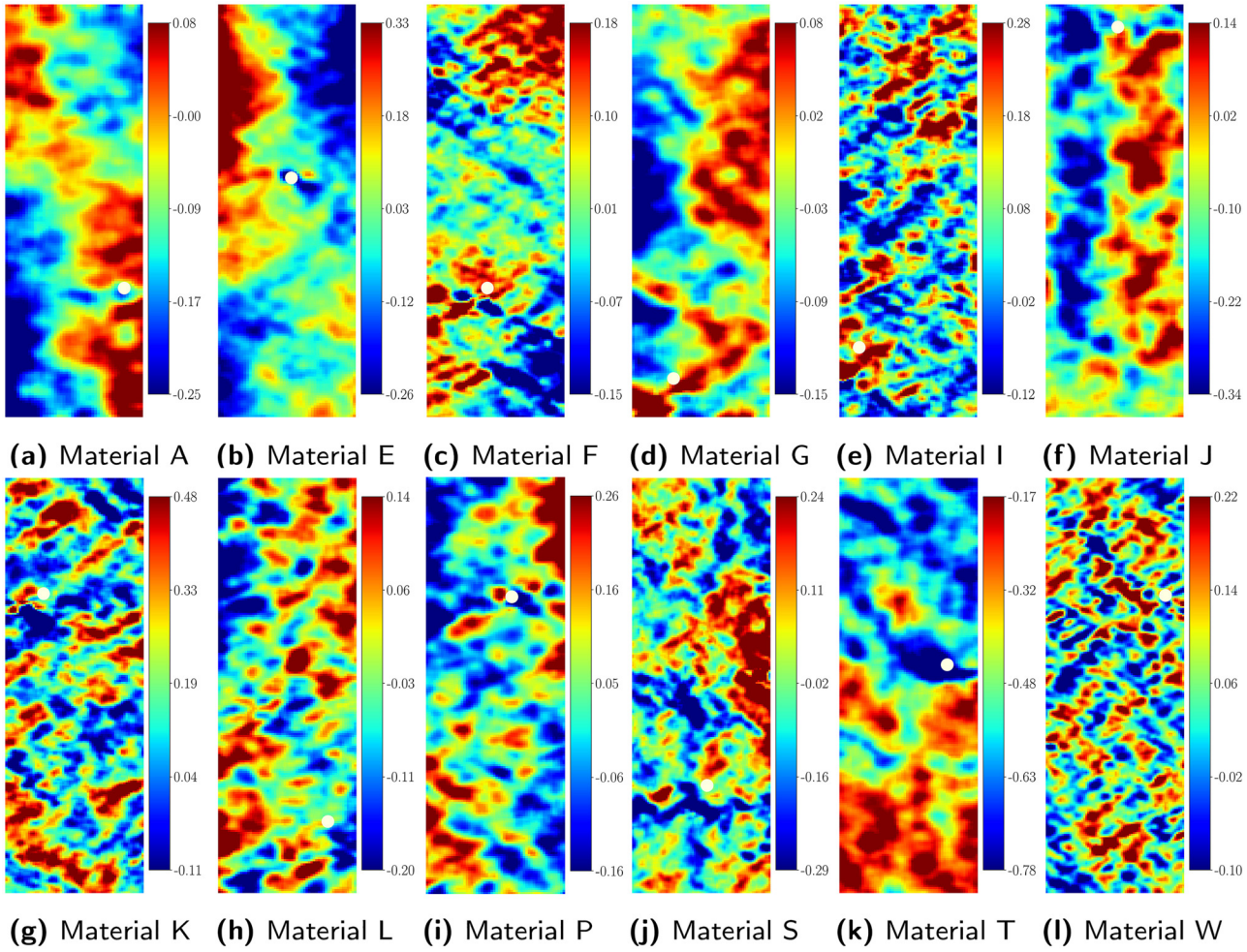

Figure 16: ε_{xy} contours for the final image before failure for these materials. Units are (%). White circle denotes initial failure location.

Materials K and W, the failure zone was experiencing relatively small strains.

We provide no analysis of post failure because that analysis is beyond the scope of this work. Tensile failure in this work was a mix of tensile buckling, with significant out-of-plane behavior, followed by fracture. Because of the out-of-plane behavior, the fracture process was an unknown mix of the three fracture modes. Furthermore, the specimen geometry and load schedule was designed for heterogeneity analysis in the linear elastic regime. Analysis of the strength behavior would require multiple size specimens, varying both width and length (Wisnom 1999). Specimen geometry, loading condition, and heterogeneity are interrelated effects. Ideally, some knowledge regarding the nature (such as size, periodicity) of the heterogeneity would guide the researcher in their selection of geometry and loading condition and number of replicates for a thorough characterization of the material. Local grammage and caliper measurements, along with size and shape of the nonuniformities, can provide some guidance, but mechanical testing is needed. An oval-shaped floc will produce different stress states when loaded in the principal direction of the floc or perpendicular to its principal direcion.

Possible failure precursors are listed Table 9; results indicate that no single factor can be used as a failure precursor. Tensile failure of these materials was complex and was not explained by any overarching mechanism. While no single factor existed for the materials examined, there may be failure precursors that exist for an individual material, and that work is part of the larger study. Failure theories, e.g., Tsai-Wu, may be applicable but cannot be examined without local knowledge of all the orthotropic stiffnesses.

Knowledge of the local orthotropic stiffnesses provides information for failure theories, but other information may also be needed. Physical heterogeneity produces stress states that can create stress concentrations, which may occur near low grammage or high grammage zones, or regions of stress intensity that occur near cracks. Analysis of materials with

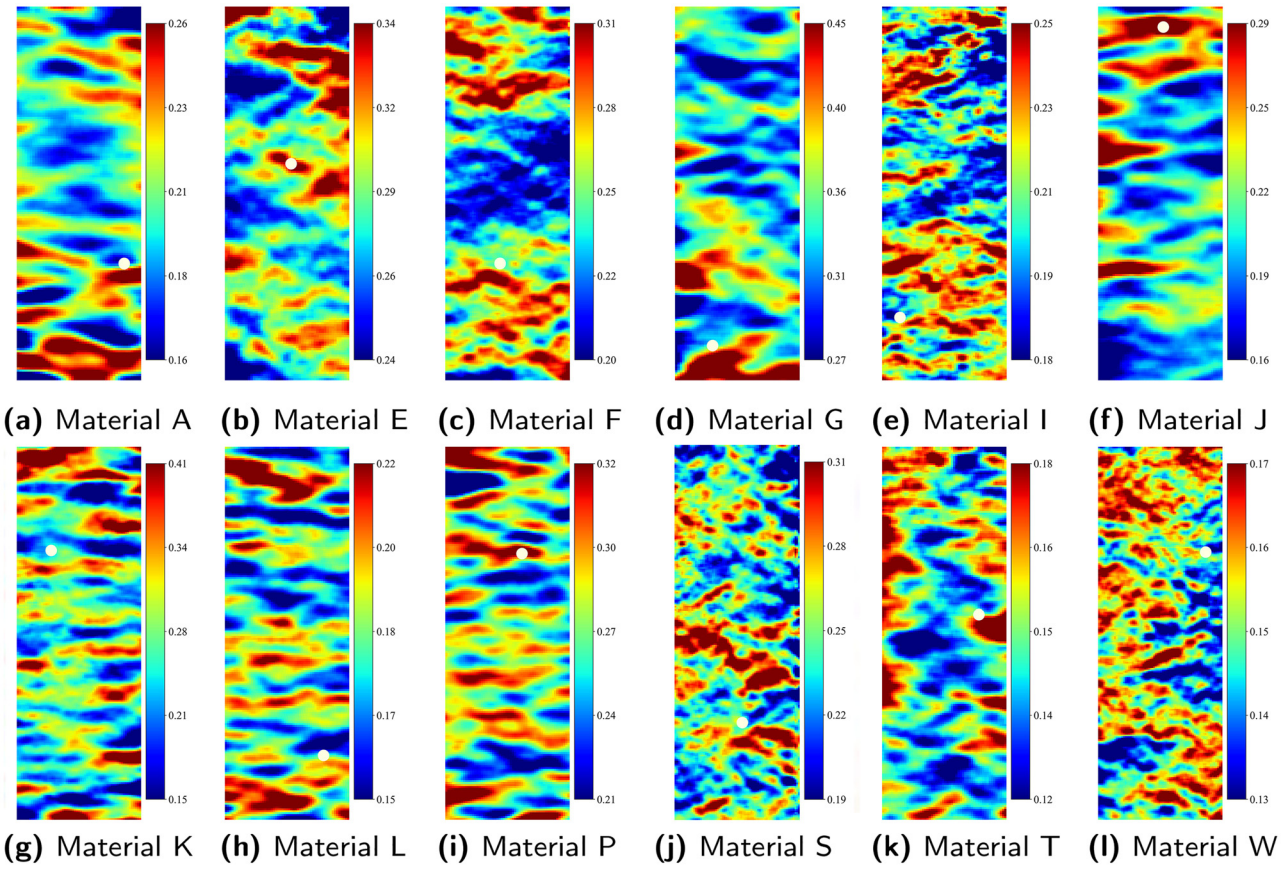

Figure 17: ε_y contours for the Cycle 5 image for these materials. Units are (%). White circle denotes initial failure location.

Table 9: Failure factors for these results. All data is for the failure zone only.

Factor	A	E	F	G	I	J	K	L	P	S	T	W
Grammage ≤ 25%-tile		x	x	x								x
Thickness ≤ 25%-tile			x	x	x	x			x			
Density > 75%-tile				x	x	x						
Density ≤ 25%-tile		x					x			x		x
$\varepsilon_{y(c)} \geq$ 75%-tile		x		x		x			x	x		
$Q_c \leq$ 25%-tile	x	x	x			x				x		

cracks requires knowledge of stress intensity factors, a material property not identified here.

6 Conclusions

This work examined the local physical heterogeneities of different commercial papers and paperboards and used inverse methodologies to identify the mechanical heterogeneities by tensile testing in the CD. Twelve different inverse analyses were employed to determine which one would create the nearest stress state to equilibrium. Both elastic and non-linear behaviors were evaluated. In all cases, the local elastic stiffness identification improved the equilibrium of the specimens as compared to assumed homogeneity.

In the elastic regime, stiffness as calculated by Fourier series expression produced the best local equilibrium in seven of the twelve materials. FEMU produced the best description of stiffness when the stiffness was nearly homogeneous or when the material had high stiffness regions scattered throughout the specimen. Thickness and density heterogeneities best described the behavior in the elastic regime; for these materials, stiffness variation was not characterized by grammage heterogeneity.

In the nonlinear, higher strain regime, stiffness identification did not produce an equilibrium state as well as it did for the elastic analysis. This poorer identification was attributed to large shear strains that could not be accommodated in the equilibrium analysis without shear stiffness identification, which was not possible in a uniaxial tensile test.

Grammage, thickness, and apparent density were unable to locate failure zones *a priori* for these materials. The larger grammages investigated here, along with the different failure mechanisms, e.g., tensile buckling, fracture, would require a more comprehensive examination of failure modes than evaluated here. A common failure mechanism may be present in a particular material and could be examined with replications.

The CD stiffness heterogeneity identified here is useful for package design by providing a rational range of safety factor selection. Furthermore, this information provides another tool for material quality evaluation related to end use performance.

Acknowledgments: The authors would like to acknowledge the efforts of Catherine Andres, Jasmine Spicer, Madeline LeBouf, Tori Jones and Jace Vu, for their assistance in conducting radiography and profilometry testing.
Research ethics: Not applicable.
Author contributions: The authors have accepted responsibility for the entire content of this manuscript and approved its submission.
Competing interests: The authors state no conflict of interest.
Research funding: None declared.
Data availability: The raw data can be obtained on request from the corresponding author.

References

Abedsoltan, H., Wood, G., and Keller, D.S. (2016). Characterization of paperboard formation using soft x-radiography and image analysis. In: TAPPI Papercon. Cincinnati OH. TAPPI Press, Atlanta.

Alzweighi, M., Mansour, R., Lahti, J., Hirn, U., and Kulachenko, A. (2021). The influence of structural variations on the constitutive response and strain variations in thin fibrous materials. *Acta Mater.* 203: 116460, https://doi.org/10.1016/j.actamat.2020.11.003.

Avril, S. and Pierron, F. (2007). General framework for the identification of constitutive parameters from full-field measurements in linear elasticity. *Int. J. Solids Struct.* 44: 4978–5002, https://doi.org/10.1016/j.ijsolstr.2006.12.018.

Borodulina, S., Kulachenko, A., Galland, S., and Nygårds, M. (2012). Stress-strain curve of paper revisited. *Nord. Pulp Pap. Res. J.* 27: 318–328, https://doi.org/10.3183/npprj-2012-27-02-p318-328.

Bossuyt, S. (2013). Optimized patterns for digital image correlation. In: *Proceedings of the 2012 annual conference on experimental and applied mechanic: imaging methods for novel materials and challenging applications*, 3. Springer, Costa Mesa, CA, USA, pp. 239–248.

Chao, Y.J. and Sutton, M.A. (1988). Measurement of strains in a paper tensile specimen using computer vision and digital image correlation. II: tensile specimen test. TAPPI J. 71: 153–156.

Considine, J.M., Pierron, F., Turner, K.T., Lava, P., and Tang, X. (2017). Smoothly varying in-plane stiffness heterogeneity evaluated under uniaxial tensile stress. *Strain* 53: e12237, https://doi.org/10.1111/str.12237.

Considine, J., Vahey, D., Evans, J., Turner, K., and Rowlands, R. (2011). Evaluation of strength-controlling defects in paper by stress concentration analyses. *J. Compos. Mater.* 46: 1323–1334, https://doi.org/10.1177/0021998311418262.

Cresson, T.M., Tomimasu, H., and Luner, P. (1990). Characterization of paper formation. i: sensing paper formation. *TAPPI J.* 73: 153–159.

Devivier, C., Pierron, F., and Wisnom, M.R. (2013). Impact damage detection in composite plates using deflectometry and the Virtual Fields Method. *Compos. Part A – Appl. S.* 48: 201–218, https://doi.org/10.1016/j.compositesa.2013.01.011.

Dias, P.A.N., Rodrigues, R.J., and Reis, M.S. (2023). Fast characterization of in-plane fiber orientation at the surface of paper sheets through image analysis. *Chemom. Intell. Lab. Syst*. 234: 104761, https://doi.org/10.1016/j.chemolab.2023.104761.

Enomae, T., Han, Y.-H., and Isogai, A. (2008). Z-directional distribution of fiber orientation of Japanese and western papers determined by confocal laser scanning microscopy. *J. Wood Sci.* 54: 300–307, https://doi.org/10.1007/s10086-008-0950-z.

Fellers, C., Andersson, H., and Hollmark, H. (1986). *The definition and measurement of thickness and density*. Marcel Dekker, New York, pp. 151–167.

Feng, C. (2012). Soft x-ray measurement of low densitymaterials and compressive response characterization. Master's thesis, Chemical and Paper Engineering. Miami University, Oxford, OH USA.

Gómez, J. and Guarín-Zapata, N. (2018). Solidspy: 2d-finite element analysis with python. https://github.com/AppliedMechanics-EAFIT/SolidsPy

Johansson, S., Engqvist, J., Tryding, J., and Hall, S.A. (2022). Microscale deformation mechanisms in paperboard during continuous tensile loading and 4D synchrotron X-ray tomography. *Strain* 58: e12414, https://doi.org/10.1111/str.12414.

Keller, D.S. and Pawlak, J.J. (2001). β-Radiographic imaging of paper formation using storage phosphor screens. *J. Pulp Pap. Sci.* 27: 117–123.

Keller, D.S., Feng, C., Bloch, J.F., and Du Roscoat, S.R. (2013). Local structural orientation of towel and tissue grades. In: I'anson, S. (Ed.). *15th Fundamental Reseasrch Symposium, Cambridge, UK*. The Pulp and Paper Fundamental Research Society, Manchester, UK, pp. 3–39.

Kerekes, R.J. and Schell, C.J. (1992). Characterization of fiber flocculation regimes by a crowding factor. *J. Pulp Pap. Sci.* 18: J32–J38.

Kerekes, R.J. and Schell, C.J. (1995). Effects of fiber length and coarseness on pulp flocculation. *TAPPI J.* 78: 133–139.

Korteoja, M.J., Lukkarinen, A., Kaski, K., Gunderson, D.E., Dahlke, J.L., and Niskanen, K.J. (1996). Local strain fields in paper. *TAPPI J.* 79: 217–224.

Krasnoshlyk, V., du Roscoat, S.R., Dumont, P., and Isaksson, P. (2018). Influence of the local mass density variation on the fracture behavior of fiber network materials. *Int. J. Solids Struct.* 138: 236–244, https://doi.org/10.1016/j.ijsolstr.2018.01.016.

Krok, P., Plew, P., and Wilk, R. (2023). Mapping the formation of paper products. Application note. Papiertechnische Stiftung (PTS) & Menlo Systems GmbH, Martinsried, Germany.

Lahti, J., Dauer, M., Keller, D.S., and Hirn, U. (2020). Identifying the weak spots in packaging paper: local variations in grammage, fiber orientation and density and the resulting local strain and failure under load. *Cellulose* 27: 10327–10343, https://doi.org/10.1007/s10570-020-03493-z.

Lyne, M.B. and Hazell, R. (1973). Formation testing as a means of monitoring strength uniformity. In *The fundamental properties of paper related to its uses, transactions of the Vth fundamental research symposium, Cambridge, UK.* FRC, Manchester, UK, pp. 74–100, 2003.

Missori, M., Conti, C., Mosca Conte, A., and Peccianti, A. (2015). Looking with Terahertz eyes. In: *Proceedings of RAIN15 – Radiazione per l'INnovazione*. INFN National Laboratories and ENEA Research Center of Frascati, Italy, October 2015. Oct 12–13.

Moffat, J.M., Beath, L.R., and Mihelich, W.G. (1973). Major factors governing newsprint strength. In: *The fundamental properties of paper related to its uses, transactions of the Vth fundamental research symposium*, Cambridge, UK, Vol. 1. The Pulp and Paper Fundamental Research Society, Manchester, UK, pp. 104–127, ISBN 0 510 45750 9.

Mohlin, U.-B. (2001). Fiber dimensions-formation and strength. *Nord. Pulp Pap. Res. J.* 16: 235–239, https://doi.org/10.3183/npprj-2001-16-03-p235-239.

Na, Y.J. and Muhlstein, C.L. (2019). Relating nonuniform deformations to fracture in uniaxially loaded non-woven fiber networks. *Exp. Mech.* 59: 1127–1144, https://doi.org/10.1007/s11340-019-00527-x.

Nguyen, T.T., Huntley, J.M., Ashcroft, I.A., Ruiz, P.D., and Pierron, F. (2014). A Fourier-series-based virtual fields method for the identification of 2-D stiffness distributions. *Int. J. Numer. Meth. Eng.* 98: 917–936, https://doi.org/10.1002/nme.4665.

Nordström, B. (2003). Effects of grammage on sheet properties in one-sided and two-sided roll forming. *Nord. Pulp Pap. Res. J.* 18: 280–287, https://doi.org/10.3183/npprj-2003-18-03-p280-287.

Norman, B. and Söderberg, D. (2001). Overview of Forming Literature, 1990-2000. In: *Trans. of the 12th Fund. Res. Symp. Oxford, 2001*. The Pulp and paper Fundamental Research Society, Manchester, UK, pp. 431–558.

Ostoja-Starzewski, M. and Castro, J. (2003). Random formation, inelastic response and scale effects in paper. *Philos. T. Roy. Soc. A* 361: 965–985, https://doi.org/10.1098/rsta.2003.1175.

Pierron, F. and Grédiac, M. (2021). Towards Material Testing 2.0. a review of test design for identification of constitutive parameters from full-field measurements. Strain 57: 1–22, https://doi.org/10.1111/str.12370.

Pierron, F. and Grédiac, M. (2012). The virtual fields method: extracting constitutive mechanical parameters from full-field deformation measurements. Springer Science & Business Media, New York, NY USA.

Sampson, W.W. (2001). The structural characterisation of fibre networks in papermaking processes—a review. In: Baker, C.F. (Ed.). *Proceedings of the transactions of 12th fundamental resource symposium, Oxford, UK*. The Pulp and Paper Fundamental Research Society, Manchester, UK, pp. 1205–1288.

Sampson, W.W. (2009). Materials properties of paper as influenced by its fibrous architecture. *Int. Mater. Rev.* 54: 134–156, https://doi.org/10.1179/174328009x411154.

Schaffnit, C., Silvy, J., and Dodson, C.T.J. (1992). Orientation density distributions of fibres in paper. *Nord. Pulp Pap. Res. J* 7: 121–125, https://doi.org/10.3183/npprj-1992-07-03-p121-125.

Sung, Y.J., Ham, C.H., Kwon, O., Lee, H.L., and Keller, D.S. (2005). Applications of thickness and apparent density mapping by laser profilometry. In: *13th Fundamental Research Symposium, Cambridge, UK*. The Pulp and Paper Fundamental Research Society, Manchester, UK, pp. 961–1007.

Sutton, M.A. and Chao, Y.J. (1988). Measurement of strains in a paper tensile specimen using computer vision and digital image correlation. I: data acquisition and image analysis system. TAPPI J. 71: 173–175.

TAPPI (2015). TAPPI T 411 om-15, Thickness of paper, paperboard, and combined board.

TAPPI (2023). TAPPI T 410 om-23, Grammage of paper and paperboard (weight per unit area).

The Mathworks, Inc. (2020). MATLAB version R2020a, Image Processing Toolbox version 11.1, Natick, Massachusetts.

Ting, T.H.D., Johnston, R.E., and Chiu, W.K. (1998). Confocal laser scanning microscope imaging of network changes in unbeaten handsheets under in-plane tensile elongation. APPITA 51: 281–286.

Villette, F., du Roscoat, S.R., Dufour, F., Bloch, J.-F., Baroth, J., and Carré, B. (2022). Toward the link between structural and mechanical properties of fiber aggregates in paper materials. *J. Mater. Sci.* 57: 7587–7599, https://doi.org/10.1007/s10853-022-07098-8.

Waterhouse, J.F., Hall, M.S., and Ellis, R.L. (1991). Strength improvement and failure mechanisms. Technical Report 2, Formation. Project 3469, A progress report to members of the Institute of Paper Science and Technology. Institute of Paper Science and Technology.

Wathén, R. and Niskanen, K. (2006). Strength distributions of running paper webs. *J. Pulp Pap. Sci.* 32: 137–144.

Wisnom, M.R. (1999). Size effects in the testing of fibre-composite materials. *Compos. Sci. Technol.* 59: 1937–1957, https://doi.org/10.1016/s0266-3538(99)00053-6.

Wong, L., Kortschot, M.T., and Dodson, C.T.J. (1996). Effect of formation on local strain fields and fracture of paper. *J. Pulp Pap. Sci.* 22: J213–J218.